RESEARCH ARTICLE

Key Points:

- We propose a three-component subgrid model consistent with the physics of two-dimensional fluids using Germano (1986, https://doi.org/10.1063/1.865568) decomposition
- The new subgrid model accurately predicts the spectral transfer of energy and enstrophy and improves a posteriori experiments
- A backscattering component (Reynolds stress) improves coarse-grid ocean models based on quasi-geostrophic and primitive equations

Correspondence to:
P. Perezhogin,
pperezhogin@gmail.com

Author Contributions:

Conceptualization: Pavel Perezhogin, Andrey Glazunov
Formal analysis: Pavel Perezhogin
Funding acquisition: Andrey Glazunov
Investigation: Pavel Perezhogin
Methodology: Pavel Perezhogin, Andrey Glazunov
Project Administration: Andrey Glazunov
Software: Pavel Perezhogin
Supervision: Andrey Glazunov
Validation: Pavel Perezhogin
Visualization: Pavel Perezhogin
Writing – original draft: Pavel Perezhogin

Subgrid Parameterizations of Ocean Mesoscale Eddies Based on Germano Decomposition

Pavel Perezhogin[1,2] and Andrey Glazunov[2]

[1]Courant Institute of Mathematical Sciences, New York University, New York, NY, USA, [2]Marchuk Institute of Numerical Mathematics, Russian Academy of Sciences, Moscow, Russia

Abstract Ocean models at intermediate resolution (1/4°), which partially resolve mesoscale eddies, can be seen as Large eddy simulations of the primitive equations, in which the effect of unresolved eddies must be parameterized. In this work, we propose new subgrid models that are consistent with the physics of two-dimensional flows. We analyze subgrid fluxes in barotropic decaying turbulence using Germano (1986, https://doi.org/10.1063/1.865568) decomposition. We show that Leonard and Cross stresses are responsible for the enstrophy dissipation, while the Reynolds stress is responsible for additional kinetic energy (KE) backscatter. We utilize these findings to propose a new model, consisting of three parts, that is compared to a baseline dynamic Smagorinsky model. The three-component model accurately simulates the spectral transfer of energy and enstrophy and improves the representation of KE spectrum, resolved KE and enstrophy decay in a posteriori experiments. The backscattering component of the new model (Reynolds stress) is implemented both in quasi-geostrophic and primitive equation ocean models and improves statistical characteristics, such as the vertical profile of eddy KE, meridional overturning circulation and cascades of kinetic and potential energy.

Plain Language Summary Ocean models at intermediate resolution contain missing physics term that accounts for the contribution of unresolved mesoscale eddies, which needs to be parameterized. Mesoscale eddies obey complex physics which should be accounted for when proposing a parameterization. Here we consider the interscale transfer of kinetic energy and enstrophy in a barotropic fluid and propose new subgrid models which capture this transfer. Our strategy is to split the subgrid contribution into three parts and propose a model for each term separately. This approach results in excellent a priori performance and improves online simulations. We demonstrate that our analysis of subgrid fluxes generalizes well across flow regimes: the new parameterization of energy redistribution improves barotropic, quasi-geostrophic and primitive equation ocean models.

1. Introduction

Classical parameterizations of mesoscale eddies are based on the ideas of Reynolds averaging where temporal or ensemble averaging is used to diagnose the effect of eddies on the mean flow (Adcock & Marshall, 2000; Eden & Greatbatch, 2008; Gent & Mcwilliams, 1990; Greatbatch, 1998; Marshall & Adcroft, 2010; Marshall et al., 2012; Wardle & Marshall, 2000). These parameterizations are the most suitable for the coarse ocean models (around 1°) where the grid resolution is insufficient to directly simulate the transient mesoscale eddies, and thus the resolved flow can be seen as a temporary mean flow. We note that the Reynolds-averaging approach relies on the spatial scale separation between the mean flow and transient eddies which is often violated in realistic ocean flows (Grooms et al., 2013). Recently, the horizontal resolution of the ocean component of climate models has increased to eddy-permitting resolution (around 1/4°, Haarsma et al. (2016)). At this resolution, the scale separation does not hold even approximately because the ocean model directly simulates the largest transient mesoscale eddies. Consequently, such resolutions are often referred to as "gray zone" (Hewitt et al., 2020).

In the gray zone, the Large eddy simulation (LES) approach is preferable (Bachman et al., 2017; Fox-Kemper & Menemenlis, 2008; Graham & Ringler, 2013; Nadiga, 2008). In the LES framework, the effect of unresolved eddies is diagnosed with a spatial filter and referred to as a subgrid forcing (Zanna & Bolton, 2020). This forcing needs to be parameterized with a subgrid model. Recently many new parameterizations of mesoscale eddies were built based on the spatial filtering approach (Bachman et al., 2017; Bolton & Zanna, 2019; Frederiksen et al., 2012; Guillaumin & Zanna, 2021; Khani & Dawson, 2023; Khani et al., 2019; Mana & Zanna, 2014; Maulik & San, 2016, 2017b; Nadiga, 2008; Pearson et al., 2017; San et al., 2013; Zanna & Bolton, 2020).

Writing – review & editing: Andrey Glazunov

The LES approach has a long history of successful applications in three-dimensional (3D) turbulence (Sagaut, 2006) and comprises a multitude of methods. The most popular subgrid model is the Smagorinsky (1963) model which relates the subgrid fluxes to the strain rate tensor. This model belongs to a class of so-called "functional models" (Sagaut, 2006). Functional models are designed to represent the mean effect of the eddies on the resolved flow. An alternative approach to subgrid modeling is "structural modeling" (Sagaut, 2006). Structural models utilize formal series expansion to approximate the subgrid forcing. Various approximations of subgrid forcing were proposed over the years: from Velocity gradient models (VGM, Clark et al. (1979)) to Scale-similarity models (SSM, Bardina et al., 1980; Bardino et al., 1983) and Approximate deconvolution models (ADM, Stolz et al. (2001)). A general approach to express the subgrid flux as an arbitrary function of velocity gradient tensor, which includes Smagorinsky and VGM models as special cases, was proposed by Pope (1975), and later extended by T. S. Lund and Novikov (1992), Wang and Bergstrom (2005); see also Anstey and Zanna (2017) in the context of the two-dimensional (2D) flows.

A linear combination of structural and functional models is referred to as a "mixed model" (Meneveau & Katz, 2000). Mixed models combine the best of both approaches: the structural part provides high correlation with the subgrid forcing and the functional part ensures the numerical stability of the simulations. Such mixed models can be naturally studied in the framework of Germano (1986) decomposition, where the subgrid stress is decomposed into Leonard, Cross and Reynolds stresses. Separate functional or structural models for each one of these stress terms are then proposed (Horiuti, 1997). We also mention another popular subgrid model in 3D LES: the "dynamic model" of Germano et al. (1991) which allows the estimation of the eddy viscosity coefficient directly from the resolved flow.

Quantifying the extent to which ocean models can benefit from the methods developed for 3D LES simulations is an open question. For example, subgrid parameterizations in 3D turbulence are mainly suited to simulate energy dissipation by the subgrid eddies (Meneveau & Katz, 2000). However, in the quasi-2D flows, the energy cascade has an inverse direction (Ferrari & Wunsch, 2009), and thus subgrid forcing energizes the flow on average. This effect is often referred to as a kinetic energy backscatter (KEB), see Thuburn et al. (2014), Jansen and Held (2014), Grooms et al. (2015), Zanna et al. (2017), Bachman et al. (2018), Bachman (2019), Jansen et al. (2019), Juricke et al. (2020, 2023), Loose et al. (2023).

Dynamic models similar to Germano et al. (1991) have been proposed for the quasi-2D flows, see San (2014), Bachman et al. (2017), Maulik and San (2017a, 2017c), Pawar et al. (2020). These models simulate only the forward energy transfer, and consequently, their consistency with the physics of the quasi-2D flows is limited. On the contrary, various structural models have been shown to simulate the backward transfer of energy, see for example, Chen et al. (2003, 2006), Bouchet (2003), Nadiga (2008), Mana and Zanna (2014), Maulik and San (2017b), Anstey and Zanna (2017), Zanna and Bolton (2020), Khani and Dawson (2023). In this paper, we apply the approach of structural modeling to represent the backward energy transfer and propose new dynamic mixed models.

The existing dynamic models in the quasi-2D fluids often suffer from a build-up of energy near the grid scale (Bachman et al., 2017; Guan, Chattopadhyay, et al., 2022; Maulik & San, 2017a, 2017c). This indicates that numerical effects may lead to large errors even in physically meaningful parameterizations (Chow & Moin, 2003; Ghosal, 1996). In particular, Thuburn et al. (2014) shows that the subgrid kinetic energy (KE) transfer diagnosed from the high-resolution data significantly depends on the choice of the numerical scheme. In this paper, we reduce discretization errors by leveraging an explicit filtering approach (Bose et al., 2010; Carati et al., 2001; Gullbrand & Chow, 2003; T. Lund, 2003; Winckelmans et al., 2001). The explicit filtering approach treats a filter width and a grid step as independent parameters. The role of discretization errors can be then reduced by enlarging a filter-to-grid width ratio (FGR, Bose et al., 2010; Chow and Moin 2003; Ghosal 1996; Meyers et al., 2003; Sarwar et al., 2017).

The goal of our study is to propose new subgrid momentum closures of ocean mesoscale eddies which are consistent with the physics of the quasi-2D flow. We analyze the enstrophy and energy fluxes in barotropic decaying turbulence using Germano (1986) decomposition. We show that the Leonard and Cross stresses describe the enstrophy dissipation, and Reynolds stress describes additional energy backscatter. Leonard stress can be computed directly. We propose a biharmonic Smagorinsky model for the Cross stress and a structural model for the Reynolds stress which is similar to Horiuti (1997). We estimate the Smagorinsky coefficient using the dynamic model of Germano et al. (1991). The energy flux produced by backscatter parameterization is

determined by considering the budget of subgrid KE (Jansen & Held, 2014) and estimation of subgrid KE (Khani & Dawson, 2023). The resulting three-component subgrid model accurately simulates energy and enstrophy fluxes and improves a posteriori experiments. Additionally, we show that the new backscatter model (Reynolds stress) improves quasi-geostrophic (QG) and primitive equation ocean models.

The study is structured as follows. In Section 2 we describe the governing equations. In Section 3 we analyze subgrid fluxes using Germano (1986) decomposition. In Section 4 we describe subgrid models. In Section 5 subgrid models are evaluated in a posteriori experiments. Section 6 is devoted to the implementation to more realistic ocean models.

2. Governing Equations

In this section, we describe a Direct numerical simulation (DNS) of decaying barotropic turbulence and numerical schemes.

The dimensionless barotropic vorticity equation in a doubly periodic domain of size $2\pi \times 2\pi$ is (Guan, Chattopadhyay, et al., 2022; Maulik & San, 2017a, 2017c):

$$\frac{\partial \omega}{\partial t} + \frac{\partial}{\partial x_j}(u_j \omega) = \frac{1}{Re}\nabla^2 \omega, \quad \nabla^2 \psi = \omega, \tag{1}$$

where x_1 and x_2 are Cartesian coordinates, $\nabla = (\partial_{x_1}, \partial_{x_2})$ is the gradient operator. We assume summation over the repeated indices ($j = 1, 2$). The relative vorticity ω, streamfunction ψ and velocity vector components u_j are related to each other as $\omega = \partial_{x_1} u_2 - \partial_{x_2} u_1$ and $(u_1, u_2) = (-\partial_{x_2}\psi, \partial_{x_1}\psi)$. The Reynolds number is defined by dimensional RMS velocity $(\widetilde{u}_{rms})$, domain size $2\pi\widetilde{L}$ and molecular viscosity $(\widetilde{\nu})$ as $Re = \widetilde{u}_{rms}\widetilde{L}/\widetilde{\nu}$.

The turbulence is initialized with a random divergence-free flow having the following KE density (per unit wavenumber k and unit area):

$$E(k) = Ak^4 \exp\left(-(k/k_p)^2\right), \quad A = \frac{4k_p^{-5}}{3\sqrt{\pi}}, \tag{2}$$

where $k_p = 10$, $k = \sqrt{k_1^2 + k_2^2}$ and k_1, k_2 are components of wavevector. The normalization constant A is chosen to set the RMS velocity to one: $u_{rms} = \left(2 \int E(k)dk\right)^{1/2} = 1$. We integrate Equation 1 with initial perturbation of form (2) until the dimensionless time $t = 10$.

In Figure 1a we show decay of the KE spectrum in the DNS simulation for a combination of parameters that we use throughout the paper: resolution $4{,}096^2$ and $Re = 512{,}000$. The spectrum is averaged over 50 realizations of the initial random field. The chosen Reynolds number is very large, and further increase of Re or resolution does not influence significantly the band of scales resolved by the coarse LES models, see squares in Figure 1b.

Both DNS and LES models are discretized with the same second-order numerical scheme, which is a typical choice in realistic ocean models (Adcroft et al., 2019; Madec & the NEMO team, 2008). Specifically, we use the Arakawa scheme on the C grid conserving energy and enstrophy (Arakawa, 1997; Maulik & San, 2017c) and second-order approximation of the Poisson equation in Equation 1 which is solved in Fourier space. A three-stage Runge-Kutta (RK3) scheme (Skamarock et al., 2008) is used for time integration, with the time step Δt satisfying the linear stability criterion CFL $= \Delta t \max_j(|u_j|)/\Delta_g < 0.7$, where Δ_g is the grid step.

3. A Priori Analysis of the Interaction With Subgrid Eddies

In this section, we diagnose the forcing produced by the subgrid eddies on the resolved flow. The analysis of subgrid forcing will guide the development of new subgrid models capable to simulate energy and enstrophy fluxes. We perform the analysis of the subgrid energy budget to propose a parameterization that is energetically consistent, see Jansen and Held (2014). Additionally, we use Germano (1986) decomposition to identify the components of subgrid forcing responsible for the energy and enstrophy fluxes.
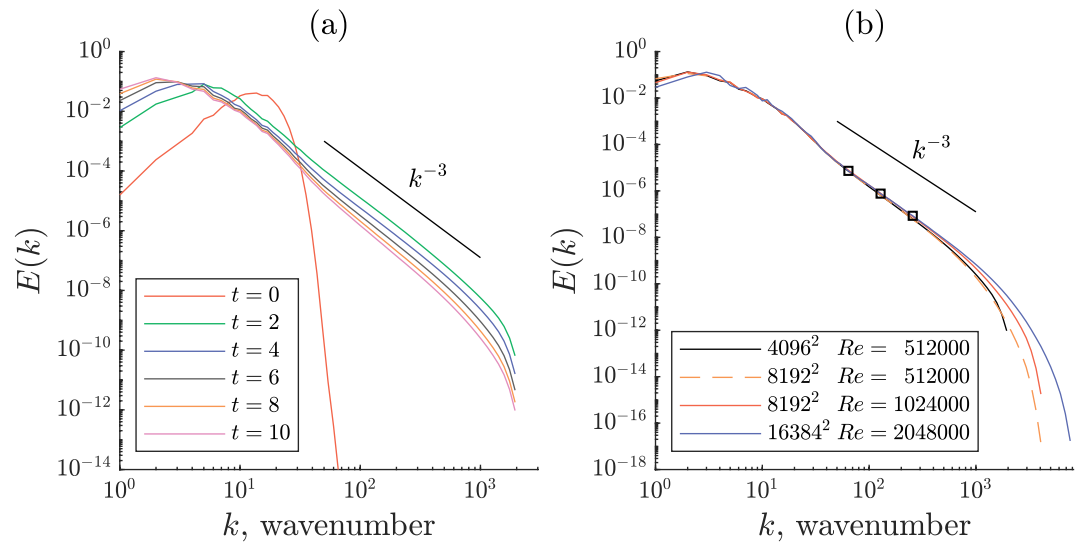
Figure 1. Kinetic energy spectrum in Direct numerical simulations: (a) time evolution at mesh $4{,}096^2$ and $Re = 512{,}000$, and (b) additional combinations of mesh and Reynolds number at $t = 10$. Squares show the cutoff wavenumber (π/Δ_g, where Δ_g—grid step) for the coarse LES models at resolutions 128^2, 256^2, and 512^2.

3.1. Filtered Equations

Following the LES approach (Sagaut, 2006), we introduce a spatial filter $\overline{(\cdot)}$ decomposing the flow into the resolved part and unresolved or subgrid eddies. The filter is Gaussian and defined in Fourier space by the transfer function $\exp\left(-\overline{\Delta}^2 k^2/24\right)$, where $\overline{\Delta}$—filter width. There are a few benefits of using the Gaussian filter. First, it has a finite second moment, and consequently, VGM and ADM approximations can be formally applied. These approximations are implicitly used in Sections 3.2 and 4.3. Second, the Gaussian filter is invertible on any finite range of scales (Langford & Moser, 1999). An invertible filter is important to apply an explicit filtering approach and to run computations with a large filter-to-grid width ratio (FGR, B1 in Appendix B).

By applying the filter to the governing Equations (1), we obtain an equation for the large-scale flow:

$$\frac{\partial \overline{\omega}}{\partial t} + \frac{\partial}{\partial x_j}\left(\overline{u}_j \overline{\omega}\right) = \frac{1}{Re}\nabla^2 \overline{\omega} - \frac{\partial}{\partial x_j}(\sigma_j), \quad \nabla^2 \overline{\psi} = \overline{\omega}, \tag{3}$$

which is unclosed and contains interaction with the subgrid eddies (subgrid flux):

$$\sigma_j = \overline{u_j \omega} - \overline{u}_j \overline{\omega}. \tag{4}$$

The spatial filter mimics the effect of a finite resolution and its width should be proportional to the grid step of the coarse LES model (Δ_g). The Gaussian filters related to the coarse resolutions of 128^2, 256^2, and 512^2 points are denoted as Δ_{128}, Δ_{256}, and Δ_{512}, respectively. We set the filter-to-grid width ratio as FGR $= \overline{\Delta}/\Delta_g = \sqrt{6}$, and explain our choice in Section 5. Note that a priori analysis is performed on a DNS grid, and the grid step of the coarse model is used only to guide the choice of the filter width $\overline{\Delta}$.

3.2. Domain-Averaged Energy Exchange With Subgrid Eddies

Kraichnan (1967), C. E. Leith (1968), and Batchelor (1969) developed a theory of the 2D forced-dissipative turbulence. Theory predicts the redistribution of enstrophy toward small scales and redistribution of energy toward large scales. Elements of this theory are observed in other quasi-2D fluids (Charney, 1971). In particular, in the 2D decaying turbulence, we observe the dissipation of enstrophy as a consequence of the direct enstrophy cascade (black line in Figure 2b) and approximate conservation of KE at a very high Reynolds number as a consequence of the inverse energy cascade (black line in Figure 2a). The KE $\left(\mathcal{E} = \frac{1}{2}u_i u_i\right)$ is given by a sum of resolved KE $\left(E = \frac{1}{2}\overline{u}_i \overline{u}_i\right)$ and subgrid KE $\left(e = \frac{1}{2}\left(\overline{u_i u_i} - \overline{u}_i \overline{u}_i\right)\right)$. Total energy conservation implies that if subgrid KE is
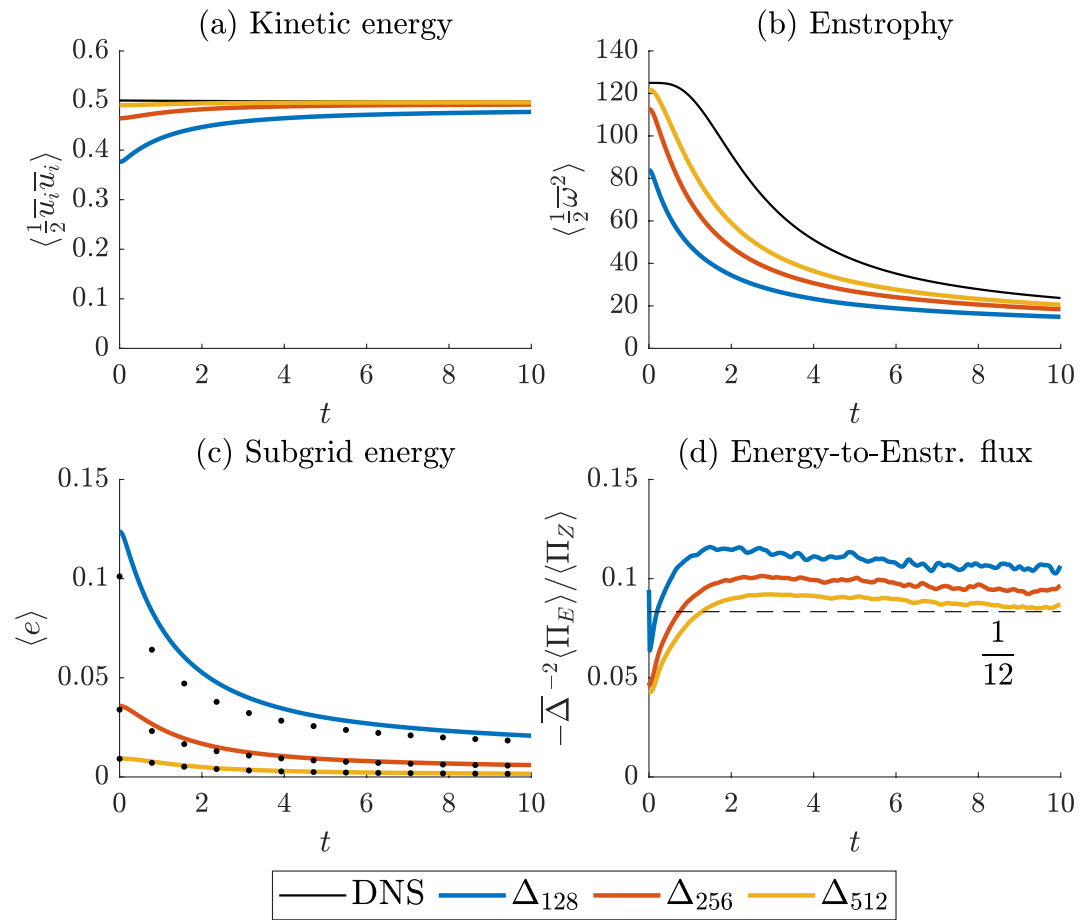
Figure 2. (a) Kinetic energy and (b) enstrophy in Direct numerical simulation (black line) and filtered solutions (in colors), (c) subgrid energy (solid lines) and its estimation according to Equation 7 in dots, (d) the ratio of energy and enstrophy fluxes; the filter is Gaussian with different widths: $\Delta_{128} > \Delta_{256} > \Delta_{512}$.

decreasing, then the resolved KE must grow, see Figures 2a and 2c. It is a consequence of the redistribution of KE toward large scales, that is, inverse energy cascade. This process is governed by the energy flux $\left(\Pi_E = \sigma_j \partial\overline{\psi}/\partial x_j\right)$ between resolved and subgrid scales and must be accurately predicted by the subgrid model. An increase in the resolved KE corresponds to negative energy flux on average and is referred to as a backscatter. In this section, we propose an estimation of the negative energy flux.

Consider the budget of subgrid KE (Equation 7 in Jansen and Held (2014)):

$$\frac{d}{dt}\langle e \rangle = \langle \Pi_E \rangle - \langle D \rangle, \tag{5}$$

where $\langle \cdot \rangle$ is the domain-averaging, $D \geq 0$ is the dissipation of subgrid KE. We have only molecular dissipation which is usually neglected (Jansen & Held, 2014; Jansen et al., 2019), that is, $D = 0$. The simplest way to predict the energy flux is to consider a statistically stationary case $\left(\frac{d}{dt}\langle e \rangle \approx 0\right)$ in Equation 5 which gives zero energy exchange between resolved and subgrid scales $\langle \Pi_E \rangle \approx 0$, see Jansen and Held (2014), Thuburn et al. (2014). This approach is not suitable for the simulation of decaying turbulence, which is not stationary. A more accurate approach would include a numerical integration of the equation analogous to Equation 5 as proposed in Jansen et al. (2015). According to Equation 5, the decrease of subgrid KE ($\frac{d}{dt}\langle e \rangle < 0$, Figure 2c) should contribute to the negative subgrid energy flux $\langle \Pi_E \rangle < 0$. That is, subgrid eddies energize the resolved eddies on average. Partee et al. (2022), Khani and Dawson (2023) proposed a new way to predict the energy of subgrid eddies: it can be estimated given the resolved flow as an alternative to the simulation of Equation 5.

The gradient model of Khani and Dawson (2023) predicts the subgrid KE using only the resolved flow as:

$$e = \frac{1}{2} \cdot \frac{\overline{\Delta}^2}{12} \frac{\partial \overline{u}_i}{\partial x_j} \frac{\partial \overline{u}_i}{\partial x_j}, \tag{6}$$

where we used a standard parameter of the gradient model for the Gaussian filter (1/12, Meneveau and Katz, 2000). In Appendix A we further show that estimation (Equation 6) is related to the resolved enstrophy $\left(Z = \overline{\omega}^2/2 \right)$ if consider spatially-averaged quantities:

$$\langle e \rangle = \frac{\overline{\Delta}^2}{12} \langle Z \rangle. \tag{7}$$

In Figure 2c we show in black dots that this model (Equation 7) accurately predicts the diagnosed subgrid KE. It allows to express the spatially-averaged energy flux through the rate of change of the resolved enstrophy:

$$\langle \Pi_E \rangle \overset{\text{Eq. (5)}}{=} \frac{d}{dt} \langle e \rangle \overset{\text{Eq. (7)}}{=} \frac{\overline{\Delta}^2}{12} \cdot \frac{d}{dt} \langle Z \rangle. \tag{8}$$

This formula resembles a common approach to estimate the energy flux ($\langle \Pi_E \rangle \approx 0$) for a statistically stationary case $\left(\frac{d}{dt}\langle Z \rangle \approx 0 \right)$, and also predicts the negative energy flux ($\langle \Pi_E \rangle < 0$) in the decaying turbulence regime $\left(\frac{d}{dt}\langle Z \rangle < 0 \right)$.

Specifically for the 2D decaying turbulence at a high Reynolds number, the resolved enstrophy can be lost only to the subgrid eddies, and thus $\frac{d}{dt}\langle Z \rangle = -\langle \Pi_Z \rangle$, where $\Pi_Z = -\sigma_j \partial \overline{\omega}/\partial x_j$ is the enstrophy flux from resolved to subgrid scales. Inserting this last expression into Equation 8, we obtain an interpretable relation between energy and enstrophy fluxes:

$$\langle \Pi_E \rangle = -\frac{\overline{\Delta}^2}{12} \langle \Pi_Z \rangle. \tag{9}$$

In Figure 2d we show that the diagnosed energy and enstrophy fluxes are directed oppositely on average, and the presented estimate of the energy flux (Equation 9) is accurate after the initial adaptation of the turbulence ($t > 1$). The formula (Equation 9) will be used to estimate a free parameter of a new backscatter parameterization. Note that Equation 8 can potentially be applied in more complicated cases of non-stationary forced turbulence but we leave this investigation for future research.

3.3. Transfer Spectra for Germano Decomposition

The subgrid energy and enstrophy transfer spectra are given by, respectively (Guan, Subel, et al., 2022):

$$T_E(k) = \sum_{|\boldsymbol{k}| \in [k, k+1)} \mathbb{R}\left(\left(\frac{\partial \sigma_j}{\partial x_j} \right)_{\boldsymbol{k}}^* (\overline{\psi})_{\boldsymbol{k}} \right), \tag{10}$$

$$T_Z(k) = \sum_{|\boldsymbol{k}| \in [k, k+1)} \mathbb{R}\left(-\left(\frac{\partial \sigma_j}{\partial x_j} \right)_{\boldsymbol{k}}^* (\overline{\omega})_{\boldsymbol{k}} \right), \tag{11}$$

and $(\cdot)_{\boldsymbol{k}}$ denotes the 2D Fourier transform, $(\cdot)^*$ is complex conjugate, $\mathbb{R}$ is real part. These transfer spectra are connected to the energy and enstrophy fluxes (Π_E, Π_Z) as follows:

$$\int T_E(k)\mathrm{d}k = -\langle \Pi_E \rangle, \quad \int T_Z(k)\mathrm{d}k = -\langle \Pi_Z \rangle. \tag{12}$$

Another simple relation is observed for barotropic flows ($\omega = \nabla^2 \psi$) and given by $T_Z(k) = T_E(k)k^2$. Although we could analyze only one of the transfer spectra ($T_Z(k)$ or $T_E(k)$), we note that factor k^2 significantly emphasizes small scales over large scales, and consequently, the most fair analysis can be made by analysis of both transfer spectra.
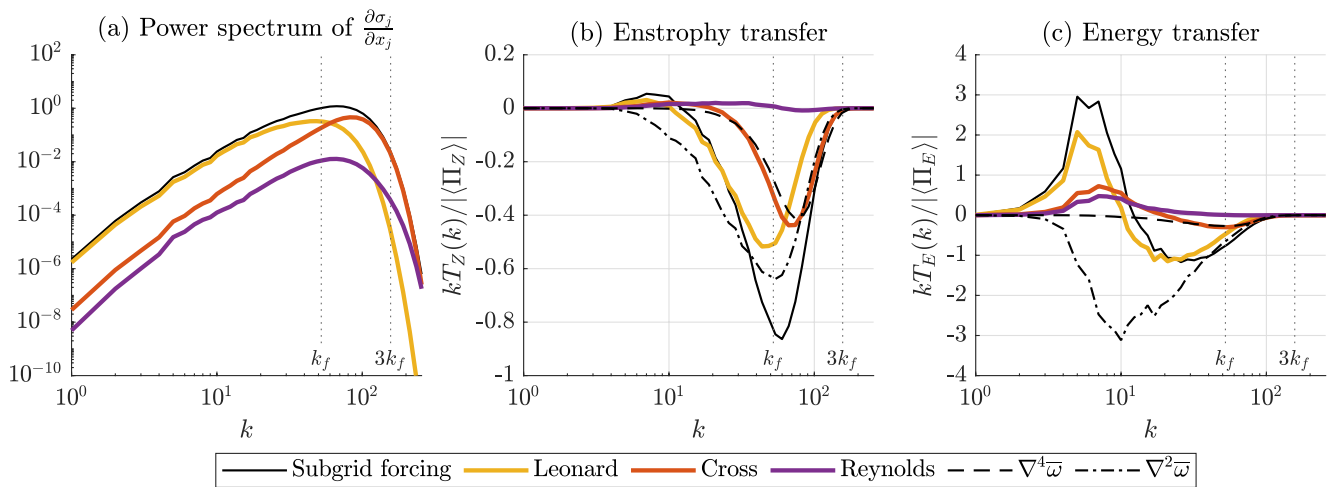
Figure 3. A priori analysis of the subgrid forcing with Germano decomposition (Equation 13) for the filter with medium width Δ_{256}, $t = 2$. (a) Power spectrum of subgrid forcing; (b) enstrophy and (c) energy transfer spectra. The filter scale is defined as $k_f = \pi/\overline{\Delta}$; $\nabla^2\overline{\omega}$ and $\nabla^4\overline{\omega}$ are dissipation spectra produced by laplacian and biharmonic eddy viscosity models.

In Figures 3b and 3c we show the transfer spectra in black line. The subgrid energy and enstrophy transfer contains a small-scale dissipative region ($T_E(k) < 0$, $T_Z(k) < 0$) and a large-scale backscatter region ($T_E(k) > 0$, $T_Z(k) > 0$), but the relative contribution of the energy backscatter is higher. We show examples of simple eddy viscosity models (dashed and dot-dashed lines in Figures 3b and 3c). These models are purely dissipative and cannot capture the complex structure of subgrid fluxes.

Many subgrid models in 3D turbulence were inspired by decomposing the subgrid stress into three parts: Leonard, Cross and Reynolds stresses (Leonard, 1975). For example, velocity gradient model (Clark et al., 1979) approximates Leonard and Cross stresses. The scale-similarity model (Bardina et al., 1980; Bardino et al., 1983) approximates Cross and Reynolds stresses. These two examples correspond to the decomposition where Leonard and Cross stresses are Galilean-non-invariant (Leonard, 1975). To retain invariance properties, we must propose a subgrid model for at least two terms simultaneously. The advantage of later suggested Germano (1986) decomposition is that every stress is Galilean-invariant and can be approximated separately. An example of a three-component model in 3D turbulence following this methodology is provided in Horiuti (1997).

The Germano (1986) decomposition of subgrid vorticity flux is given by Nadiga (2008):

$$\sigma_j = \underbrace{\overline{\overline{u}_j\overline{\omega}} - \overline{\overline{u}}_j\overline{\overline{\omega}}}_{\text{Leonard}} + \underbrace{\overline{\overline{u}_j\omega'} + \overline{u'_j\overline{\omega}} - \overline{\overline{u}}_j\overline{\omega'} - \overline{u'_j}\ \overline{\overline{\omega}}}_{\text{Cross}} + \underbrace{\overline{u'_j\omega'} - \overline{u'_j}\ \overline{\omega'}}_{\text{Reynolds}},$$

(13)

where primed quantities denote subgrid eddies, $\omega' = \omega - \overline{\omega}$ and $u'_j = u_j - \overline{u}_j$. The Reynolds stress represents the effect on the resolved flow from eddy-eddy interactions, Cross stress represents the effect of eddy-resolved flow interactions. Finally, the Leonard stress contains only the resolved fields and can be directly computed given $\overline{u}_j$ and $\overline{\omega}$.

In Figure 3 we show the spectral content for each component in the Germano decomposition. The enstrophy dissipation is mostly represented by Leonard and Cross stresses, see Figure 3b. Also, the enstrophy dissipation by the Cross stress can be approximated by the biharmonic viscosity model ($\nabla^4\overline{\omega}$), see the dashed line in Figure 3b. These findings will be used to propose a mixed dissipative model of subgrid forcing. The KEB is influenced by Leonard, Cross and Reynolds stresses, but only the Reynolds stress almost purely represents the positive energy transfer (Figure 3c), and this property will be used to propose a new backscatter model. The contribution of Germano decomposition components to the energy and enstrophy transfer is similar for the other filter widths.

We briefly mention how the choice of the filter influences the spectral properties of the Germano decomposition. We found that Box and Gaussian filters produce similar transfer spectra. Using the cut-off filter considerably changes the small-scale enstrophy dissipation produced by the Cross term: it becomes highly scale-selective

(Frederiksen & Davies, 1997). The energy transfer spectrum for the Reynolds stress is roughly similar for all three filters (Box, Gaussian and cut-off). Finally, the Leonard stress for the cut-off filter equals zero in the *resolved scales* defined as wavenumbers below the Nyquist frequency of the cut-off filter.

4. Subgrid Models

In this section, we describe the dynamic Smagorinsky model (DSM) and propose new dissipative and backscattering models by applying the results of a priori analysis.

4.1. Dynamic Smagorinsky Model (DSM)

The DSM is a popular baseline subgrid model in the quasi-2D turbulence research (Frezat et al., 2022; Guan, Chattopadhyay, et al., 2022; Maulik & San, 2017a; Pawar et al., 2020). The Smagorinsky eddy viscosity model is given by:

$$\sigma_j \approx \sigma_j^{DSM} = -C_S^2 \overline{\Delta}^2 |\overline{S}| \frac{\partial \overline{\omega}}{\partial x_j}, \tag{14}$$

where C_S is the Smagorinsky coefficient. Filtered strain-rate tensor is $\overline{S}_{ij} = \frac{1}{2}\left(\partial_{x_j} \overline{u}_i + \partial_{x_i} \overline{u}_j\right)$ and its modulus $|\overline{S}| = \sqrt{2\overline{S}_{ij}\overline{S}_{ij}}$. In the dynamic model of Germano et al. (1991), a free parameter (C_S) is estimated from the resolved turbulent flux $l_j = \widehat{\overline{u_j}\overline{\omega}} - \widehat{\overline{u}}_j \widehat{\overline{\omega}}$, where a new test filter $\widehat{(\cdot)}$ of width $\widehat{\Delta}$ is introduced. The resolved turbulent flux can be decomposed as follows (Germano identity):

$$l_j = \Sigma_j - \widehat{\sigma}_j, \tag{15}$$

where $\Sigma_j = \widehat{\overline{u_j}\overline{\omega}} - \widehat{\overline{u}}_j \widehat{\overline{\omega}}$ is the subgrid flux with respect to the combined filter $\widehat{\overline{(\cdot)}}$. Substituting Smagorinsky model (Equation 14) to the Germano identity (Equation 15) and applying the least squares procedure of Ghosal et al. (1995), we determine the Smagorinsky coefficient:

$$C_S^2 = \frac{\langle l_j \alpha_j \rangle}{\langle \alpha_j \alpha_j \rangle}, \tag{16}$$

where $\langle \cdot \rangle$ is the spatial averaging and

$$\alpha_j = -\widehat{\overline{\Delta}}^2 |\widehat{\overline{S}}| \frac{\partial \widehat{\overline{\omega}}}{\partial x_j} + \overline{\Delta}^2 \widehat{|\overline{S}| \frac{\partial \overline{\omega}}{\partial x_j}}. \tag{17}$$

The derivation of Equations 16 and 17 is provided in C1 in Appendix C. In B2 in Appendix B, we show that in the 2D turbulence, the dynamic modeling of the subgrid vorticity flux has advantages compared to the dynamic modeling of the subgrid stress which is a common approach in the 3D turbulence (Germano et al., 1991).

We set the width of the Gaussian base $\overline{(\cdot)}$ and test $\widehat{(\cdot)}$ filters equal $\left(\widehat{\Delta} = \overline{\Delta}\right)$ similarly to Brun and Friedrich (2001) instead of a popular choice $\widehat{\Delta} > \overline{\Delta}$ (Germano, 1992). It is possible because we avoid an often-used simplifying assumption $\widehat{\overline{\Delta}} \approx \widehat{\Delta}$ (Brun & Friedrich, 2001; San, 2014). Instead, the width of the combination of Gaussian filters is computed directly as $\widehat{\overline{\Delta}} = \sqrt{\overline{\Delta}^2 + \widehat{\Delta}^2} = \sqrt{2}\,\overline{\Delta}$ (Brun & Friedrich, 2001; Germano, 1992). As long as the filter width ratio satisfies $\widehat{\overline{\Delta}}/\overline{\Delta} > 1$, there is no division by zero in the denominator of Equation 16 and dynamic procedure can be formally applied (Brun & Friedrich, 2001). We found our approach $\left(\widehat{\Delta} = \overline{\Delta}\right)$ more convenient. In particular, it allows us to reduce the number of free parameters and use as wide base and test filters as possible having only a three-point stencil. Note also that the only parameter of the base filter which is used in the DSM model is the filter width $\overline{\Delta}$. We treat this parameter independently from the grid step $\left(\overline{\Delta} \neq \Delta_g\right)$ and thus we follow the explicit filtering approach (Carati et al., 2001). Subgrid models presented in the following sections will use the base filter $\overline{(\cdot)}$ directly in scale-similarity and Reynolds stress parts.
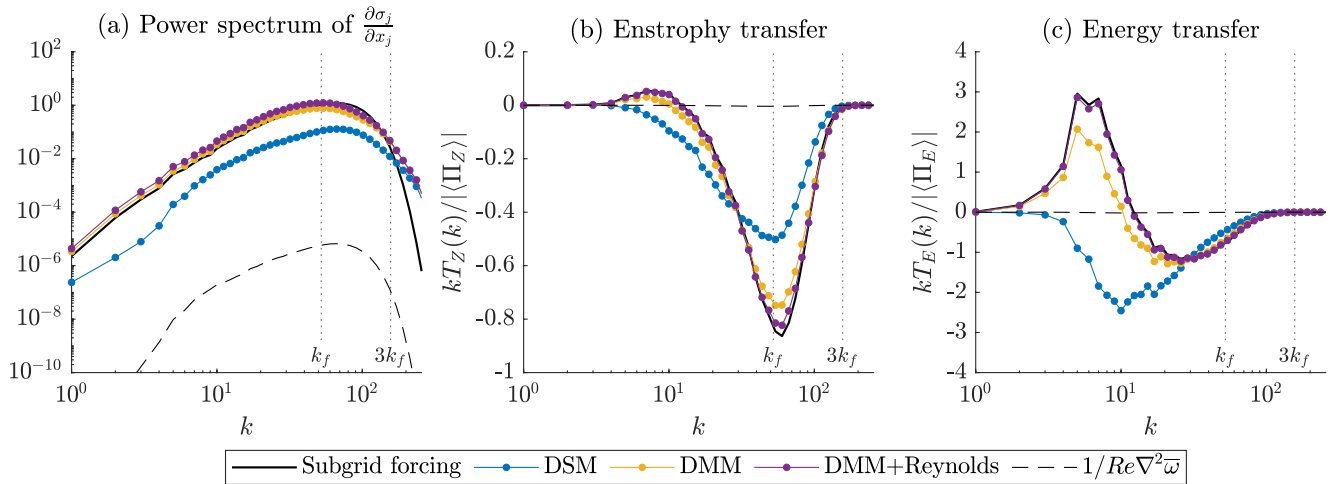
Figure 4. A priori analysis of subgrid models: DSM is dynamic Smagorinsky model, Dynamic Mixed Model (DMM) comprises Leonard stress, DMM + Reynolds includes an additional backscatter parameterization (Reynolds stress). Medium filter width Δ_{256} and $t = 2$. Subgrid models are computed given the filtered Direct numerical simulation (DNS) data on the grid of DNS. Dashed line shows contribution of the molecular viscosity at $Re = 512,000$.

The spectral properties of the DSM model (Equations 14 and 16) in a priori analysis are shown in Figure 4. The DSM is a purely dissipative model, and it predicts the enstrophy dissipation of the subgrid forcing reasonably well (Figure 4b). However, it introduces the dissipation of KE on large scales, where the subgrid forcing has a significant positive transfer, that is, backscatter (Figure 4c). Thus we conclude that DSM model is inconsistent with the physics of the quasi-2D fluids, and it needs to be modified.

4.2. Dynamic Mixed Model (DMM)

We first leverage the approach of mixed models (Meneveau & Katz, 2000) to model the dissipation of enstrophy. The classical mixed model combines Leonard stress (also known as the scale-similarity model, SSM, Bardina et al., 1980) with the laplacian Smagorinsky eddy viscosity model (Guan, Subel, et al., 2022). However, we have shown in a priori analysis that the enstrophy dissipation is accurately represented by the combination of the Leonard stress with biharmonic eddy viscosity. We utilize this finding in the mixed model as follows:

$$\sigma_j^{DMM} = \overline{\overline{u_j}\,\overline{\omega}} - \overline{\overline{u}_j}\,\overline{\overline{\omega}} + C_S^4 \overline{\Delta}^4 |\overline{S}| \frac{\partial\left(\nabla^2\overline{\omega}\right)}{\partial x_j}, \tag{18}$$

and dynamic procedure to determine the Smagorinsky coefficient:

$$C_S^4 = \frac{\langle (l_j - h_j)\alpha_j \rangle}{\langle \alpha_j \alpha_j \rangle}, \tag{19}$$

where

$$\alpha_j = \widehat{\overline{\Delta}}^4 |\widehat{\overline{S}}| \frac{\partial \nabla^2 \widehat{\overline{\omega}}}{\partial x_j} - \overline{\Delta}^4 \widehat{|\overline{S}| \frac{\partial \nabla^2 \overline{\omega}}{\partial x_j}} \text{ and } h_j = \widehat{\overline{\overline{u}_j}\,\widehat{\overline{\omega}}} - \widehat{\overline{\overline{u}}_j}\,\widehat{\overline{\overline{\omega}}} - \left(\widehat{\overline{\overline{u_j}\,\overline{\omega}}} - \widehat{\overline{\overline{u}_j}\,\overline{\overline{\omega}}}\right). \tag{20}$$

The derivation of Equations 19 and 20 is provided in C2 in Appendix C; see also Vreman et al. (1994) for explanation of h_j.

The a priori analysis with the DMM model (Equations 18 and 19) shows an improvement in the enstrophy dissipation spectrum, power spectrum and KE backscattering in large scales, see Figure 4. However, the positive energy transfer on large scales by the DMM model is clearly underestimated, and it needs to be further modified to account for the missing backscatter.
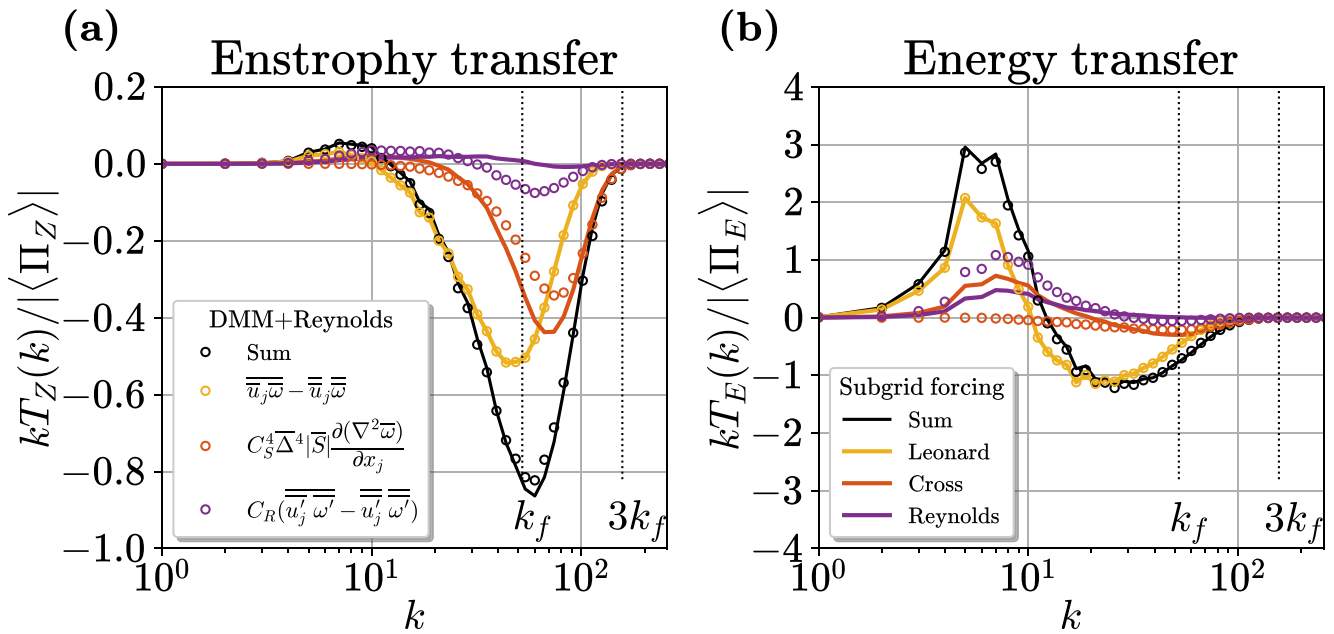
Figure 5. A priori analysis of DMM + Reynolds model. Solid lines show components of the subgrid forcing, and circles show components of the subgrid model. Medium filter width Δ_{256} and $t = 2$.

4.3. DMM With Backscattering Part (DMM + Reynolds)

We have shown in a priori analysis that the Reynolds stress is a promising candidate for an additional backscatter model: it has a small contribution to the enstrophy budget and almost purely represents a positive transfer of KE. The Reynolds stress cannot be computed given the filtered fields $\overline{\omega}$ and $\overline{u}_j$, but can be approximated as follows:

$$\overline{u_j' \omega'} - \overline{u_j'}\,\overline{\omega'} \approx \sigma_j^{KEB} = \overline{\overline{u_j'}\,\overline{\omega'}} - \overline{\overline{u_j'}}\,\overline{\overline{\omega'}}, \tag{21}$$

where $\overline{u_j'} = \overline{u}_j - \overline{\overline{u}}_j$ and $\overline{\omega'} = \overline{\omega} - \overline{\overline{\omega}}$, see Horiuti (1997) for details. The modification to DMM model accounting for an additional backscatter then reads:

$$\sigma_j = \sigma_j^{DMM} + C_R \sigma_j^{KEB}, \tag{22}$$

where σ_j^{DMM} and its parameter C_S are set in the previous section. The energy balance Equation 9 reads as $\langle \sigma_j \partial\overline{\psi}/\partial x_j \rangle = \frac{\overline{\Delta}^2}{12}\langle \sigma_j \partial\overline{\omega}/\partial x_j \rangle$, and allows to choose a free parameter C_R as follows:

$$C_R = -\frac{\langle \sigma_j^{DMM} \beta_j \rangle}{\langle \sigma_j^{KEB} \beta_j \rangle}, \tag{23}$$

where

$$\beta_j = \frac{\partial\overline{\psi}}{\partial x_j} - \frac{\overline{\Delta}^2}{12}\frac{\partial\overline{\omega}}{\partial x_j}. \tag{24}$$

The proposed DMM + Reynolds model (Equations 22 and 23) demonstrates excellent a priori results: it is same good as the DMM model in reproducing the power spectrum and enstrophy dissipation (Figures 4a and 4b), but additionally improves KEB on large scales (Figure 4c). The transfer spectra for each component of DMM + Reynolds subgrid model in comparison to components of Germano decomposition are shown in Figure 5. The scale-similarity part $\left(\overline{\overline{u}_j\overline{\omega}} - \overline{\overline{u}}_j\overline{\overline{\omega}}\right)$ is exactly the Leonard stress by construction. The biharmonic Smagorinsky model $\left(C_S^4\overline{\Delta}^4|\overline{S}|\frac{\partial(\nabla^2\overline{\omega})}{\partial x_j}\right)$ captures only the enstrophy dissipation part of the Cross stress. The Reynolds stress model $\left(C_R\left(\overline{\overline{u_j'}\,\overline{\omega'}} - \overline{\overline{u_j'}}\,\overline{\overline{\omega'}}\right)\right)$ captures the energy backscatter of both Reynolds and Cross stress.
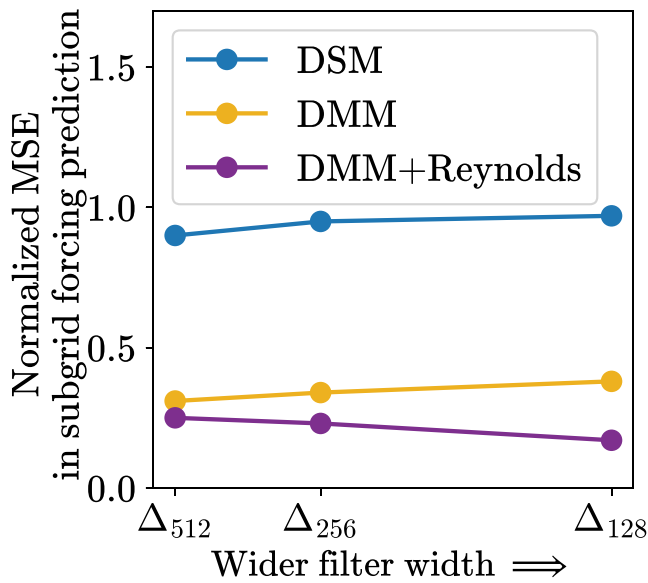
Figure 6. Mean squared error (MSE) in a priori analysis of subgrid models on Direct numerical simulation grid, averaged over $t \in [2, 10]$. Error at a single time is: $\text{MSE} = \left\langle \left(\partial_{x_j} \sigma_j - \partial_{x_j} \sigma_j^m \right)^2 \right\rangle / \left\langle \left(\partial_{x_j} \sigma_j \right)^2 \right\rangle$, where σ_j is the subgrid flux and σ_j^m is a subgrid model.

So we emphasize that although the Germano decomposition inspired the development of the three-component model, the component wise representation of the Cross and Reynolds stresses is less accurate than the representation of their joint contribution.

The proposed modifications to the dynamic Smagorinsky model (DMM and DMM + Reynolds) significantly improve the Mean squared error (MSE) in the prediction of subgrid forcing, see Figure 6. We emphasize that the improvement due to including the parameterization of Reynolds stress increases as the filter gets wider, which is expectable because subgrid and Reynolds stresses should be equal for a very large filter width (Jakhar et al., 2023; Sullivan et al., 2003).

4.4. Numerical Discretization of Subgrid Models

We discretize the subgrid models (DSM, DMM, and DMM + Reynolds) with the second-order numerical schemes. The spatial Gaussian filter is implemented in Fourier space if $\epsilon = \overline{\Delta}/\Delta_g > \sqrt{6}$ and using second-order approximation otherwise (Sagaut & Grohens, 1999):

$$\overline{\phi} = \frac{1}{24}\epsilon^2(\phi_{j+1} + \phi_{j-1}) + \left(1 - \frac{\epsilon^2}{12}\right)\phi_j, \tag{25}$$

where j is an index of a grid node in one direction. The 2D discrete filter is given by a sequential application of one-dimensional filters (Equation 25) along x_1 and x_2 directions, that is, filter product, see Sagaut and Grohens (1999). A combination of filters $\widehat{\overline{(\cdot)}}$ is given by a sequential application of the base and test filters. The only tunable parameter remains in the coarse LES models: filter-to-grid width ratio $\overline{\Delta}/\Delta_g$, and we discuss it in the next section.

5. A Posteriori Experiments

In this section, we implement the proposed subgrid models into the LES Equation 3, and perform a posteriori experiments. The goal for LES models is to reproduce filtered DNS (fDNS) data on a coarse grid.

5.1. Comparison of Subgrid Models

As a reference solution, we use DNS at resolution $4,096^2$ and $Re = 512,000$. In order to demonstrate that the proposed subgrid models do not generate numerical noise, we integrate LES Equation 3 on a coarse grid without molecular viscosity $\left(\frac{1}{Re}\nabla^2\overline{\omega} = 0\right)$. Note that results with molecular viscosity are almost identical. We also provide simulations with unparameterized model ($\sigma_j = 0$), where the only dissipation is related to the time integration scheme (RK3). Neglecting molecular viscosity is a common practice in realistic ocean models, and in our case it is justified by its low impact on scales of the coarse LES models, see Figures 1 and 4.

Every experiment is computed for an ensemble of 50 realizations. Numerical integration starts at $t = 1$, and the initial condition is prepared from DNS data as follows. We first apply a Gaussian filter of width $\overline{\Delta}$ to DNS fields, and then perform spectral truncation of wavenumbers $|k_i| > \pi/\Delta_g$, where Δ_g is the grid step of a coarse LES model. We run a posteriori experiments for three resolutions (128^2, 256^2, 512^2) at a fixed FGR: $\overline{\Delta}/\Delta_g = \sqrt{6}$. This parameter was chosen based on the sensitivity studies and corresponds to a tradeoff between the strength of the discretization errors and the number of directly resolved turbulent eddies, see B1 in Appendix B.

All the proposed dynamic models (DSM, DMM, DMM + Reynolds) produce numerically stable solutions without build-up of energy spectrum near the grid scale for a range of resolutions, see upper row in Figure 7. The most evident difference between the subgrid models is observed in reproducing the KE level (Figure 7, middle row). The DSM model falsely predicts energy decay, the DMM model is almost energy conservative, and only the DMM + Reynolds model is able to predict energy growth in accordance with fDNS data. The most significant
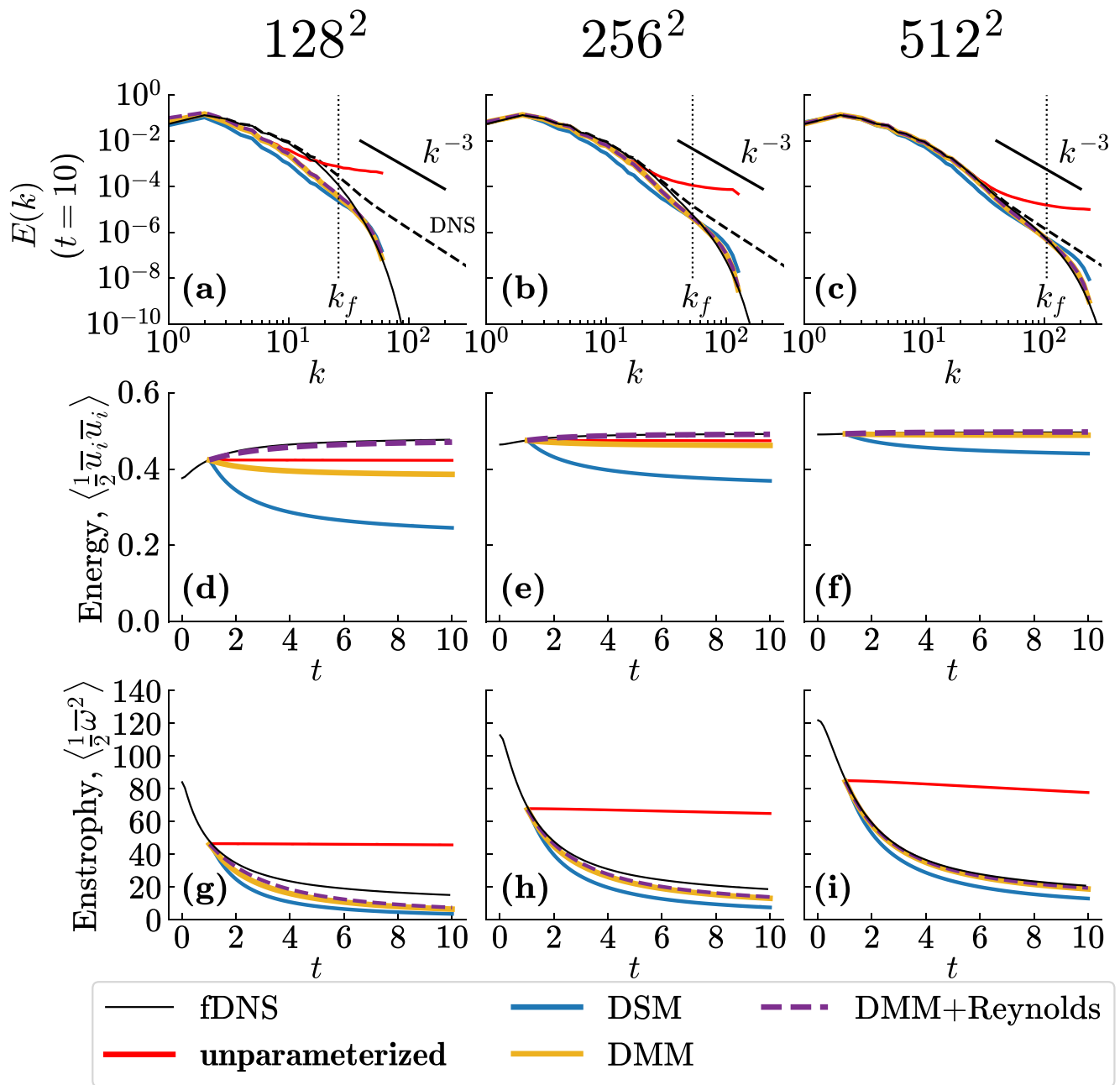
Figure 7. A posteriori experiments with subgrid models integrated with zero viscosity $\left(\frac{1}{Re}\nabla^2\overline{\omega} = 0\right)$; unparameterized simulation ($\sigma_j = 0$) shows the dissipation introduced by the time integration scheme. Upper row: spectrum of kinetic energy (KE) at $t = 10$, middle row: KE, bottom row: enstrophy. Direct numerical simulation at resolution $4{,}096^2$ and $Re = 512{,}000$ is used as a reference solution.

effect of the Reynolds stress on the energy level is observed for coarser resolutions in accordance with a priori analysis. The energetic effect can be studied further by considering PDFs of local energy and enstrophy fluxes (Figure 8, middle and lower rows). Mixed models (DMM and DMM + Reynolds) predict local fluxes of either sign contrary to the DSM model which is purely dissipative. At coarser resolutions, the DMM + Reynolds model predicts heavier tails on both sides of the distributions, that is, has stronger dissipation and backscatter of energy and enstrophy compared to the DMM model.

The mixed models (DMM and DMM + Reynolds) are better than the baseline (DSM) in many characteristics. They improve the KE spectrum shape near the filter scale k_f (Figure 7, upper row), they demonstrate less
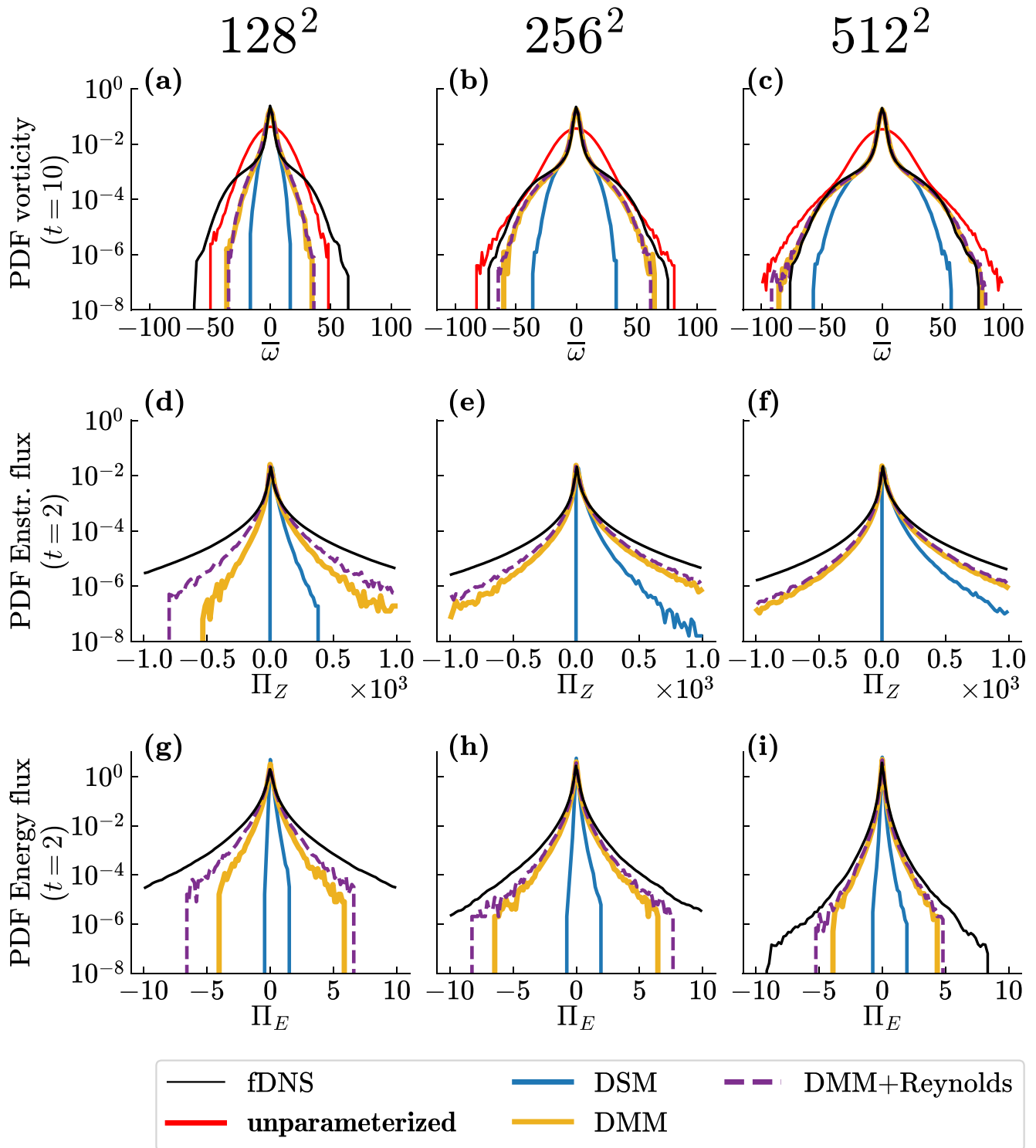
Figure 8. Upper row: PDF of vorticity at final time $t = 10$, middle row: PDF of enstrophy flux $\Pi_Z = -\sigma_j \frac{\partial \overline{\omega}}{\partial x_j}$ at $t = 2$, where $\Pi_Z < 0$ corresponds to backscatter, lower row: PDF of energy flux $\Pi_E = \sigma_j \frac{\partial \overline{\psi}}{\partial x_j}$ at $t = 2$, where $\Pi_E < 0$ corresponds to backscatter. Fluxes Π_Z and Π_E are computed in a posteriori experiments.

dissipation of the enstrophy (Figure 7, lower row), and improve tails of vorticity PDF (Figure 8, upper row). We emphasize however that while improvement of DMM model over DSM model is evident in all characteristics, the improvement of DMM + Reynolds model compared to DMM model is observed only in the total energy level and
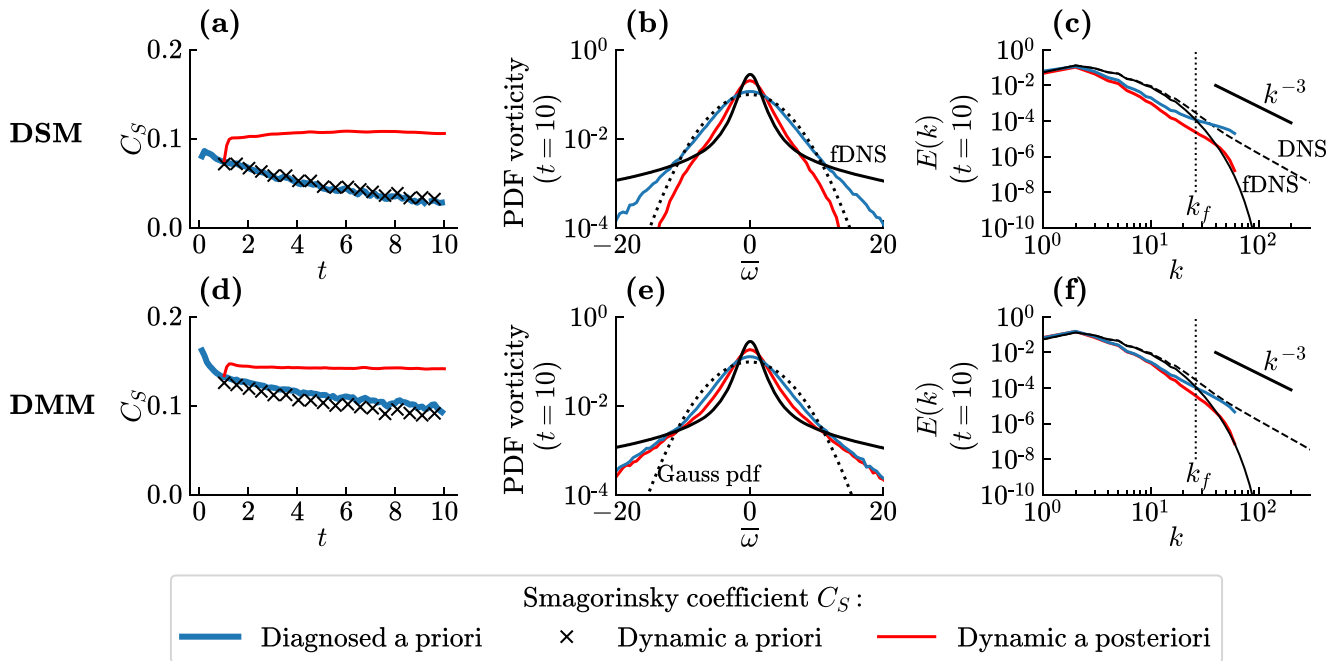
Figure 9. Left column: comparison of the predicted and diagnosed Smagorinsky coefficient (C_S). Blue line: C_S diagnosed from Direct numerical simulation (DNS) data. Cross(×): prediction of C_S by a dynamic model on filtered DNS data. Red line: prediction by a dynamic model in a posteriori experiment. Two rightmost columns: vorticity PDF and energy spectrum in a posteriori experiments with corresponding C_S. Upper row: dynamic Smagorinsky model, lower row: Dynamic Mixed Model. All experiments have $Re = 512,000$ and the widest filter width Δ_{128}.

local energy/enstrophy fluxes. Additional energy in DMM + Reynolds model at the coarsest resolution simply accumulates on the largest scales instead of energizing small coherent eddies. Although somewhat unimportant in decaying turbulence, we emphasize that accurate prediction of KE is essential in complex baroclinic flows and directly influences many other statistics (Jansen & Held, 2014).

5.2. Scale Invariance

We observe that all subgrid models have similar defects at the coarsest resolution: they overly dissipate enstrophy, they have diminished tails in vorticity PDF and they have reduced KE density in the middle scales (Figures 7a, 7g, and 8a). In this case, the filter width corresponds to not a self-similar part of the energy spectrum (Figure 7a), and consequently, the filter width is roughly equal to the size of coherent eddies.

Dynamic subgrid models are built on the assumption that the Smagorinsky coefficient is scale-invariant, that is, it is independent of the filter width. However, this assumption violates whenever we deal with a break of self-similarity of the energy spectrum. For this case, a scale-dependent dynamic model was proposed (Meneveau & Lund, 1997; Porté-Agel et al., 2000). Likewise, the scale invariance of the Smagorinsky model can be violated for the quasi-2D flows exhibiting the enstrophy cascade, and for this case C. Leith (1996) proposed a new eddy viscosity model (Bachman et al., 2017; Fox-Kemper & Menemenlis, 2008). A break of the scale invariance of the Smagorinsky model can potentially lead to an inaccurate prediction of the Smagorinsky coefficient by the dynamic procedure of Germano et al. (1991) and consequent overly enstrophy dissipation.

In Figure 9a, we show in blue line the Smagorinsky coefficient (C_S) diagnosed from the DNS data by the least squares fit of the subgrid flux σ_j:

$$C_S^2 = \frac{\langle \sigma_j \alpha_j \rangle}{\langle \alpha_j \alpha_j \rangle}, \quad \alpha_j = -\overline{\Delta}^2 |\overline{S}| \frac{\partial \overline{\omega}}{\partial x_j}. \tag{26}$$

The subgrid model DSM applied to filtered DNS data (Equation 16) accurately predicts the diagnosed parameter C_S, see Cross(×) in Figure 9a. However, once we evaluate the subgrid model a posteriori, the Smagorinsky coefficient abruptly increases (red line in Figure 9a) and it results in the excessive dissipation of enstrophy. We

conclude that the scale invariance of the eddy viscosity model has a minor effect on the accuracy of the dynamic procedure, but the main difficulty is in the lack of consistency between a priori and a posteriori performance of the same subgrid model (Ross et al., 2023). In Figures 9b and 9c we compare the Smagorinsky model with the coefficient diagnosed from DNS data (blue line) and estimated dynamically (red line). The blue line indicates a substantial amount of numerical noise: vorticity PDF becomes close to Gaussian and energy accumulates near the grid scale with middle scales remaining unchanged. Thus we conclude that the dynamic procedure predicts a coefficient that is optimal for a posteriori performance. Similar conclusions can be made about the DMM model, which is shown in the lower row of Figure 9. Analogous analysis for the DMM + Reynolds model involves two coefficients and for brevity is given in Appendix D.

5.3. Dynamic Two-Parameter DMM + Reynolds Model

The DMM + Reynolds model accurately predicts the total energy level, and it is a consequence of the energetically-consistent estimation of the free coefficient C_R. In particular, our estimation procedure (Equation 8) allows us to guarantee that the energy contribution of subgrid parameterization is bounded at any time moment T as follows:

$$\int_0^T -\langle \Pi_E \rangle dt \leq \left. \frac{\overline{\Delta}^2}{12} \langle Z \rangle \right|_{t=0}. \tag{27}$$

The Equation 8 can potentially be used in more complex flows, however, it still contains physical assumption (dissipation of subgrid KE is zero) and it is non-local in time (derivative d/dt should be somehow approximated). In Appendix D, we show that both parameters C_S and C_R can be estimated simultaneously using the two-parameter dynamic procedure. Although this approach cannot guarantee bounded growth of KE, a posteriori experiments show a remarkable resemblance with the original DMM + Reynolds model proposed in Section 4.3.

6. Reynolds Stress in QG and Primitive Equation Ocean Models

The most unexpected outcome of our study of the subgrid fluxes in the 2D decaying turbulence was the role of the Reynolds stress tensor in energizing the flow on large scales. The role of Reynolds stress in 3D turbulence is different: it dissipates energy in spectral space (Horiuti, 1997; Schilling & Zhou, 2002; Thiry & Winckelmans, 2016). The backscattering property of the Reynolds stress cannot be guaranteed theoretically and depends on the underlying flow. Note that the energy backscatter is essential in baroclinic ocean models and responsible for the correct reproducing of the KE and many other statistical properties (Jansen & Held, 2014; Juricke et al., 2019). Thus, the overall performance of the three-component model depends on the efficiency of the Reynolds stress model to simulate the backscatter in realistic ocean flows.

In this section, we implement only a part of the DMM + Reynolds model (Reynolds stress parameterization) into ocean models based on the QG and primitive equations and show that it can reproduce the energy backscatter. For simplicity, we choose the coefficient C_R manually. Implementation of the full three-component model is deferred for future studies.

6.1. Two-Layer QG Model

We use an idealized QG ocean model (pyqg, Abernathey et al., 2022). Our configuration is called "eddy" and described in Ross et al. (2023), P. Perezhogin et al. (2023). The model has two fluid layers in a doubly-periodic domain. It is forced by the prescribed vertical shear of a zonal flow and loses its energy by frictional dissipation in the bottom layer. The spatial discretization is accomplished with the pseudo-spectral method. The dissipation of enstrophy and numerical noise is provided by the highly scale-selective exponential filter which multiplies the Fourier coefficients of the potential vorticity (PV) after every time step by the following function: $e^{-23.6(\Delta x)^4(\kappa-\kappa_c)}$ in range of wavenumbers $\kappa > \kappa_c = 0.65\pi/\Delta x$. All numerical experiments presented in this section include the described dissipation mechanism.

We extend the Reynolds model (Equation 21) to simulate the subgrid flux of PV as follows:

$$\frac{\partial q}{\partial t} = \cdots - C_R \frac{\partial}{\partial x_j} \left(\overline{u'_j \, q'} - \overline{u'_j} \, \overline{q'} \right), \tag{28}$$
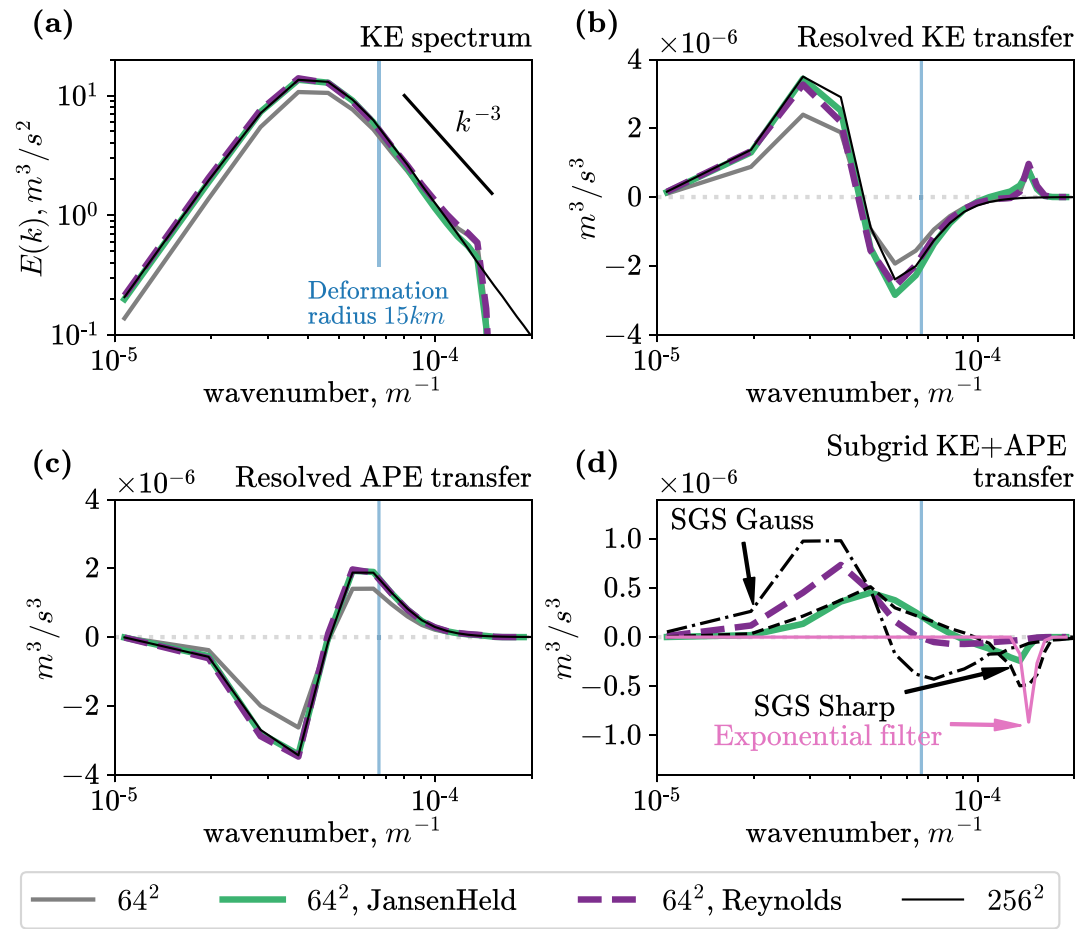
Figure 10. Experiments in two-layer quasi-geostrophic idealized ocean model. High-resolution simulation (256^2) is compared to models at coarse resolution, where 64^2 denotes unparameterized simulation, JansenHeld denotes negative viscosity backscatter, and Reynolds is given in Equation 28. (a) kinetic energy (KE) spectrum, (b) resolved transfer of KE, (c) resolved transfer of available potential energy, (d) transfer of total energy by subgrid parameterizations.

where q and u_j are the resolved PV and velocity on a coarse grid; $q' = q - \overline{q}$ and $u'_j = u_j - \overline{u_j}$. Note that we omitted one filtering operation in Equation 28 for clarity of numerical implementation (see Section 1.3 in Layton and Rebholz (2012)). The filter $\overline{(\cdot)}$ is Gaussian with $\overline{\Delta}/\Delta_g = 2$. The parameterization is applied layerwise with the same C_R which controls the strength of energy injection. We manually selected $C_R = 7$ by matching the KE spectrum on large scales for high-resolution and coarse parameterized models.

We choose the parameterization of Jansen and Held (2014), Jansen et al. (2015) as a baseline subgrid model. Implementation details are provided in Ross et al. (2023), and we choose the optimal parameters of the parameterization from this paper. JansenHeld subgrid model consists of two parts: small-scale dissipation parameterized by biharmonic viscosity and larger-scale backscatter parameterized by laplacian operator with negative viscosity.

In Figure 10 we compare coarse models on a grid 64^2 (grid step 15.6 km) to the high-resolution simulation (256^2, 3.9 km) after reaching statistical equilibrium: we average the results between 5 and 20 years of the simulation for an ensemble of 10 members. The energy cycle comprises two cascades (Salmon, 1978; Vallis, 2017). The available potential energy (APE) is redistributed toward smaller scales following the direct cascade (Figure 10c), where it is converted to the KE near the Rossby deformation radius. The KE is redistributed toward larger scales following the inverse cascade (Figure 10b). The coarse model fails to simulate the energy transfer, and its KE spectral density is smaller compared to the high-resolution model (Figure 10a). Both backscatter parameterizations (Reynolds and JansenHeld) simulate the energy injection in the large scales (Figure 10d) and amplify the resolved (i.e., unparameterized) cascades of KE and APE (Figures 10b and 10c), which results in a significant improvement in the reproducing of the KE spectrum.

In Figure 10d we show the energy transfer produced by subgrid models in a posteriori experiments in comparison to the subgrid forcing diagnosed a priori, see P. Perezhogin et al. (2023). The negative viscosity parameterization (JansenHeld) is suitable for the Sharp filter on large scales (see Kraichnan (1976) for explanation), and the Reynolds parameterization is closer to the subgrid forcing diagnosed with the Gaussian filter. Note that we show the joint contribution of laplacian backscatter and biharmonic dissipation for JansenHeld model, but the contribution of Reynolds parameterization is shown alone. The laplacian part of JansenHeld model returns energy on all scales up to the grid scale, and consequently, the biharmonic part is required to shift the backscattering region toward larger scales. On the contrary, the Reynolds stress model returns energy on scales larger than the deformation radius and consequently can be used without biharmonic dissipation (in this QG model). Note that in both cases there is an additional drain of energy due to the exponential filter, see pink line in Figure 10d. We conclude that JansenHeld backscatter model is more scale selective and can energize the flow in smaller scales compared to the Reynolds backscatter model. This difference can be seen as an advantage or disadvantage depending on the application. For example, in realistic ocean simulations, the laplacian backscatter model is often smoothed to return energy on larger scales (Juricke et al., 2019). The following section shows a case where a scale-selective backscatter may be preferable.

6.2. Primitive Equation Ocean Model NEMO

We use the primitive equation ocean model NEMO (Madec & the NEMO team, 2008) in the Double Gyre configuration (Lévy et al., 2010). The model contains 30 vertical layers in a domain with a flat bottom and vertical walls. The circulation is forced by the prescribed wind stress and buoyancy fluxes on the surface; the equation of state is linear and comprises temperature and salinity. The reference model has grid step 1/9° (11.7 km) with coarse models having grid steps 1/3° (35.3 km) and 1/4° (26.5 km). Every simulation starts from the snapshot of 1° model which was spun up for 1,000 years. Then every model is integrated for 120 further years with 20 last years used for the collection of statistics. An analog of Jansen and Held (2014) backscatter parameterization in NEMO ocean model was implemented by the author (P. Perezhogin, 2019; P. A. Perezhogin, 2020). We use the optimal parameters of the parameterization from these papers. Note that the biharmonic viscosity represents the only small-scale enstrophy dissipation mechanism in the three types of coarse ocean models differing in the backscattering part of the parameterization. Biharmonic viscosity has a constant coefficient equal to (m^4 s^{-1} units): 10^{12}, $5 \cdot 10^{11}$, and $5 \cdot 10^{10}$ for 1/3°, 1/4°, and 1/9° models, respectively.

We extend the Reynolds parameterization (Equation 21) to simulate the subgrid momentum flux as follows:

$$\frac{\partial u_i}{\partial t} = \cdots - \frac{\partial}{\partial x_j}\left(C_R \left(\overline{u_i' u_j'} - \overline{u_i'}\ \overline{u_j'} \right) \right), \quad i, j \in \{1, 2\}, \tag{29}$$

where u_i is the resolved horizontal velocity on a coarse grid and $u_i' = u_i - \overline{u_i}$. The parameterization is applied layerwise with the same C_R. We observed that if C_R is tuned to improve the KE, the wider filter $\overline{(\cdot)}$ allows choosing the lower parameter C_R. Consequently, we define the filter $\overline{(\cdot)}$ as two iterations of the three-point filter (Equation 25) with maximum allowable $\epsilon = \sqrt{6}$. The three-point filter imposes physical boundary conditions on the velocity: no-normal flow and free slip. In preliminary experiments, we observed that attenuating the Reynolds parameterization near the boundaries qualitatively improves the results. Note that the JansenHeld parameterization appeared to work fine without such attenuation. We introduce the attenuation of Reynolds parameterization smoothly in the vicinity of the wall ($l \leq L$) as follows: $C_R \to C_R \cdot (1 - \cos(\pi l/L))/2$, where l is the distance to the wall and L is the length scale of attenuation. After some tuning, we set L as four grid steps. The only remaining free parameter $C_R = 30$ was simply tuned to obtain the best Root Mean Squared Errors (RMSE) in the vertical profile of eddy kinetic energy (EKE) at resolution 1/4°. We note that C_R was increased substantially compared to QG case because the small-scale dissipation was changed to less scale selective, and consequently, more energy needs to be returned back. The chosen C_R is only slightly larger than in the barotropic turbulence case (Appendix D).

The Reynolds model works as a backscatter parameterization and energizes the flow on a coarse grid. Similarly to the JansenHeld subgrid model, the EKE can be increased near the surface and the bottom, see Figure 11a. Both backscatter parameterizations were tuned for 1/4° resolution, and it is clear that the energy level at 1/3° resolution is a bit lower. We hope that one of the considered procedures for the a posteriori estimation of parameter C_R in the Reynolds backscatter model can improve generalization in future studies. The spatial spectrum indicates
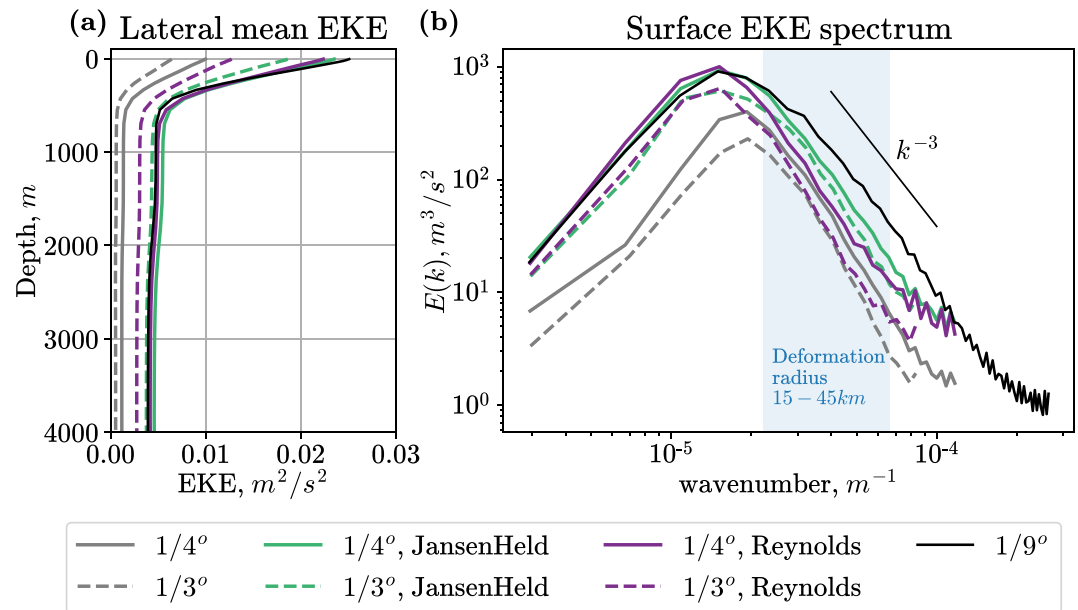
Figure 11. Experiments in NEMO ocean model in Double Gyre configuration. (a) 20-year mean eddy kinetic energy (EKE) averaged laterally over the whole domain. (b) Spatial spectrum of surface EKE (half the power spectrum of velocity deviations from 1-year mean flow).

an increase in EKE density for Reynolds parameterization in many resolved scales with the JansenHeld model reproducing EKE spectrum slightly better in the middle scales, see Figure 11b.

An improvement in the representation of the resolved eddy activity results in an improvement in several other metrics. In Figure 12 we show 20-year mean sea surface temperature (SST) for the reference simulation and errors for coarse models. The largest error for the unparameterized model is concentrated near the western boundary (Figure 12a) and is explained by the misrepresentation of the western boundary current (WBC, Lévy et al. (2010)). Both backscatter parameterizations improve the mean SST near the western boundary (Figures 12b and 12c), but the Reynolds model is also better in the northern region (Figure 12c). The RMSE in surface fields for temperature and salinity indicates lower errors for the Reynolds model, see Table 1. In Figure 13 we show 20-year mean meridional overturning circulation (MOC) streamfunction (Cabanes et al., 2008). Both backscatter parameterizations improve the streamfunction near the latitude of WBC separation (∼30°N), but Reynolds parameterization is also better in improving the northern circulation cell (∼45°N). Additionally, we show that both backscatter parameterizations significantly improve the resolved eddy meridional heat flux near the latitude ∼30°N (see Figure 13).

7. Conclusions

In this work, we perform careful a priori analysis of energy and enstrophy fluxes in the 2D decaying turbulence and develop mixed subgrid parameterizations based on previous studies (Germano, 1986; Germano et al., 1991; Horiuti, 1997; Vreman et al., 1994), but in the context of the 2D fluids. We evaluate these parameterizations in a posteriori experiments for a range of resolutions and implement the Reynolds part of the new parameterization to the QG and primitive equation ocean models.

Our main contributions and findings are as follows:

- We consider the budget of subgrid KE (Jansen & Held, 2014) and estimation of subgrid KE (Khani & Dawson, 2023) to predict the domain-averaged KE flux produced by subgrid eddies. It extends an ad hoc approach ($\langle \Pi_E \rangle \approx 0$) suitable for statistically stationary flows to nonstationary flows via $\langle \Pi_E \rangle = \frac{\overline{\Delta}^2}{12} \cdot \frac{d}{dt} \langle Z \rangle$. Note that testing this new formula requires further research in baroclinic models.
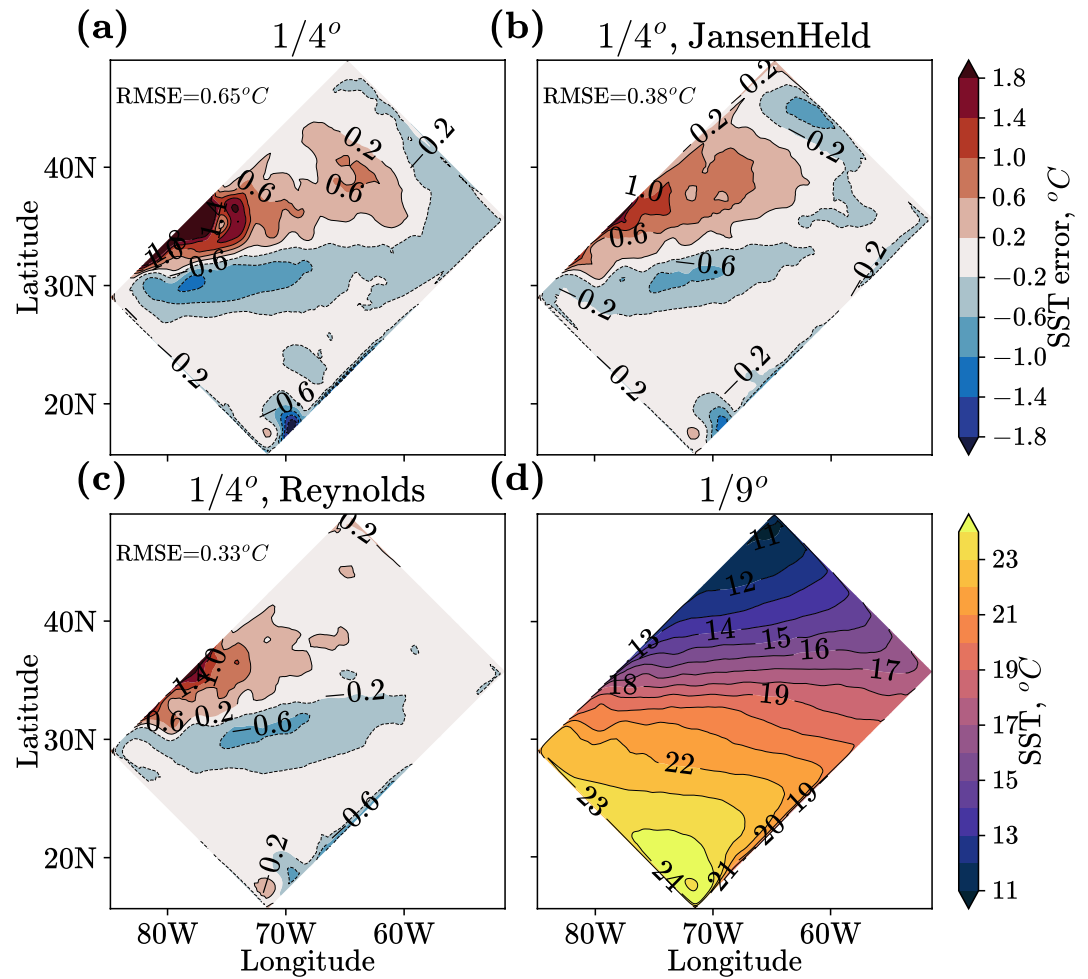
Figure 12. Experiments in NEMO ocean model. (d) 20-year mean sea surface temperature (SST) in the high-resolution model; (a–c) errors in SST for coarse models. The Reynolds-parameterized model in panel (c) is given in Equation 29.

- The components of Germano decomposition play a special role in forming energy and enstrophy subgrid fluxes: Leonard and Cross stresses are responsible for the enstrophy dissipation; all three stresses (Leonard, Cross, Reynolds) contribute to the KEB in large scales, but only the Reynolds stress produces almost positive-definite KE transfer.

- We start from the DSM in a priori analysis and show by gradual changes how to build a subgrid model which correctly simulates energy and enstrophy fluxes. In particular, we simulate the enstrophy dissipation by the Leonard stress and the biharmonic Smagorinsky model which approximates the Cross stress; an approximation to the Reynolds stress is used to simulate a missing backscatter of KE.

- The new subgrid parameterization (DMM + Reynolds) is numerically stable at zero molecular viscosity. It improves the reproduction of the KE spectrum, PDF of vorticity and decay of enstrophy. The new method to estimate the subgrid energy flux allows to reproduce the growth of the resolved KE at a very high Reynolds number.

- We additionally showed that instead of energetically-consistent tuning of the backscattering coefficient (C_R), we can estimate C_R using a fully dynamic approach (Appendix D) which does not include any physical assumptions except of scale similarity.

Table 1
The Root Mean Squared Errors (RMSE) in 20-Year Mean Sea Surface Height (SSH), Sea Surface Temperature (SST) and Sea Surface Salinity (SSS)

	SSH (m)	SST (°C)	SSS (psu)
1/4°	0.108	0.647	0.128
1/4°, JansenHeld	0.054 (−49.7%)	0.383 (−40.7%)	0.11 (−13.9%)
1/4°, Reynolds	0.058 (−46.0%)	0.327 (−49.5%)	0.088 (−31.4%)
1/3°	0.121	0.943	0.178
1/3°, JansenHeld	0.092 (−24.3%)	0.643 (−31.8%)	0.174 (−2.6%)
1/3°, Reynolds	0.099 (−18.3%)	0.596 (−36.8%)	0.123 (−31.2%)

Note. The error is computed w.r.t. 1/9° model.

Figure 13. Experiments in NEMO ocean model. In contours: meridional overturning circulation (MOC) streamfunction computed as $\Psi_{MOC} = \int_{-H}^{z} \int_{west}^{east} \langle V \rangle_t \, dx \, dz$ in Sverdrups, where $\langle V \rangle_t$−20-year mean meridional velocity. In color: the resolved meridional eddy heat flux, defined as zonal integral of $\rho_0 C_p (\langle TV \rangle_t - \langle T \rangle_t \langle V \rangle_t)$, see P. A. Perezhogin (2020).

- The role of the Reynolds stress model as a KEB parameterization holds in two additional ocean models: pseudospectral QG model and finite volume primitive equation model NEMO. Similarly to the Jansen and Held (2014) backscatter parameterization, the Reynolds model allows to energize the flow and improves various statistical properties, such as KE spectrum, the vertical profile of EKE, interscale KE and APE transfers, the resolved meridional eddy heat flux, MOC and errors in surface fields, such as SST, Sea Surface Salinity and Sea Surface Hight.

The important result of our analysis in the decaying turbulence problem is the absence of free physical parameters in the proposed subgrid parameterizations. The only parameter that was tuned a posteriori is the filter-to-grid width ratio (FGR) which was shown to control the relative importance of the numerical discretization errors. We expect that the DMM model can be extended to more complex ocean models by considering analogous formulation in momentum equations. Implementation of the full DMM + Reynolds model would require proposing a procedure for determining the C_R coefficient. In this paper, we considered three approaches: estimation based on the energetic principles and dynamic two-parameter model in decaying turbulence, and simple tuning in QG and NEMO ocean models. Importantly, C_R can be easily tuned manually, and in our experiments with the NEMO ocean model, we showed it can be chosen uniquely for all depths and spatial locations.

We would like to explain the difference between DMM + Reynolds model and the subgrid model proposed for 3D turbulence in Horiuti (1997). The differences are rather minor: we approximate the vorticity flux instead of the momentum flux and use the biharmonic Smagorinsky model instead of the laplacian one. As we show in Appendix D, a two-parameter dynamic procedure similar to Horiuti (1997) can be applied for the 2D flows as well. The role of the Reynolds stress tensor differs in 2D and 3D fluids: the Reynolds stress energizes the flow

in the 2D case but dissipates energy in the 3D case (Schilling & Zhou, 2002). It is promising that the parameterization of the Reynolds stress does not rely on the physical assumptions and can be applied in both cases. Finally, we would like to note that a probable application of the model may be the simulation of 3D turbulent flows with strong quasi-2D structure.

Additional future studies related to Germano decomposition can allow us to gain new insights on subgrid modeling. For example, we have shown that the role of the Reynolds stress model increases as the filter gets wider, as it is seen in the a priori MSE metric, simulation of resolved KE a posteriori, and better results in the northern region in NEMO ocean model, where Rossby deformation radius falls within subgrid scales. Consequently, new subgrid parameterizations for coarse models can be based on the prediction of the Reynolds stress instead of the full subgrid forcing, see for example, in the context of machine learning (Bolton & Zanna, 2019; Zanna & Bolton, 2020). We demonstrated that the most severe discrepancy between predicted and diagnosed Smagorinsky coefficient comes not from the lack of scale invariance, but from a difference between a priori and a posteriori performance of the same dynamic model. We suggest that the crudest approximation in our DMM + Reynolds model comes from the representation of the Cross stress. New accurate models of the Cross stress could potentially improve the consistency of a priori and a posteriori experiments, and gain a posteriori performance.

Appendix A: Relation Between Subgrid Energy and Resolved Enstrophy

We decompose velocity gradient tensor $\frac{\partial \overline{u}_i}{\partial x_j}$ into symmetric $\overline{S}_{ij}$ and antisymmetric $\overline{\Omega}_{ij}$ parts, and consequently $\frac{\partial \overline{u}_i}{\partial x_j} \frac{\partial \overline{u}_i}{\partial x_j} = \overline{S}_{ij}\overline{S}_{ij} + \overline{\Omega}_{ij}\overline{\Omega}_{ij} = |\overline{S}|^2/2 + \overline{\omega}^2/2$ (Borue & Orszag, 1998). Up to the boundary conditions, the spatial averaging $\langle \cdot \rangle$ can be used to show that $\langle |\overline{S}|^2 \rangle = \langle \overline{\omega}^2 \rangle$ (Buxton et al., 2011). Finally, the estimation of subgrid KE (Equation 6) is related to the resolved enstrophy $\left(Z = \overline{\omega}^2/2 \right)$ in spatially-averaged sense:

$$\langle e \rangle = \frac{1}{2} \cdot \frac{\overline{\Delta}^2}{12} \langle \frac{\partial \overline{u}_i}{\partial x_j} \frac{\partial \overline{u}_i}{\partial x_j} \rangle = \frac{\overline{\Delta}^2}{12} \langle Z \rangle. \tag{A1}$$

Appendix B: Approaches to Reduce the Generation of Numerical Noise Near the Grid Scale

The dynamic models in the quasi-2D turbulence often struggle to predict a sufficient enstrophy dissipation and lead to the formation of the numerical noise near the grid scale; see examples in Bachman et al. (2017), Maulik and San (2017c), Guan, Chattopadhyay, et al. (2022). In this Appendix, we consider two approaches to reduce the numerical noise generation.

B1. Eliminating Discretization Errors With the Explicit Filtering Approach

The discretization errors may be an important source of discrepancies between a priori and a posteriori performance. In this work, we apply the explicit filtering approach to reduce the role of numerical errors (Gullbrand & Chow, 2003). The main idea of explicit filtering consists in considering the grid step of the coarse model Δ_g and filter width $\overline{\Delta}$ as independent parameters. Fixing the filter width $\overline{\Delta}$ and enlarging the FGR = $\overline{\Delta}/\Delta_g$, it is possible to eliminate the discretization errors from the LES Equation 3.

In Figure B1 we show the energy spectrum in a posteriori experiments with the DMM model at a fixed filter width and enlarging FGR (and corresponding grid resolution). At low resolution (FGR = 2) we observe a build-up of energy density near the grid scale, and at larger FGRs coarse models converge to the filtered solution. There is a tradeoff between the strength of discretization errors and the number of directly simulated degrees of freedom (Bose et al., 2010; T. Lund, 1997, 2003; Sarwar et al., 2017). We use as small FGR as possible to better utilize the grid resolution, but large enough to reduce the role of discretization errors. An optimal FGR for the DMM model is FGR = $\sqrt{6}$ which we use in a posteriori experiments for all three subgrid models (DMM, DMM + Reynolds, DSM).
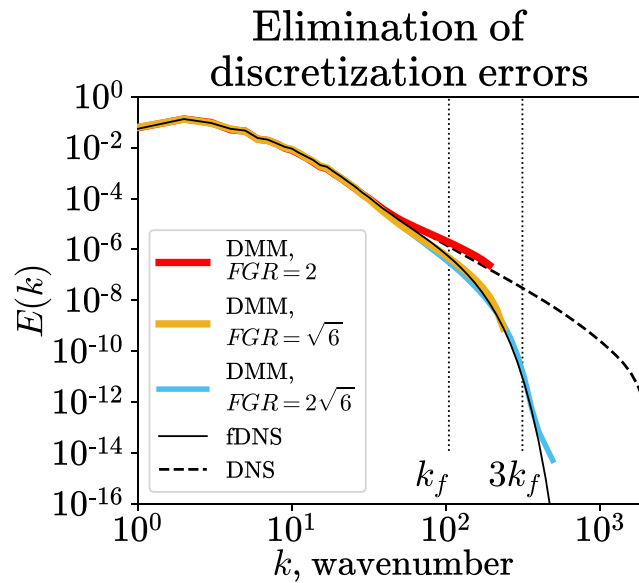
Figure B1. Eliminating discretization errors in a posteriori experiments by enlarging the $FGR = \overline{\Delta}/\Delta_g$ parameter, where filter width is fixed $\left(\overline{\Delta} = \Delta_{512}\right)$ and grid step is varying; $t = 10$. Experiments with FGR equal to 2, $\sqrt{6}$ and $2\sqrt{6}$ have resolutions 418^2, 512^2, $10{,}24^2$, respectively.

B2. Additional Formulations of the DSM Model

The DSM model proposed in Section 4 approximates the subgrid vorticity flux σ_j. The corresponding Germano identity reads as $l_j = \Sigma_j - \widehat{\sigma}_j$. There are many variations of the DSM model in the 2D turbulence research. For example, the Germano identity for the subgrid stress can be used (Germano et al., 1991; Guan, Chattopadhyay, et al., 2022; Pawar et al., 2020):

$$L_{ij} = T_{ij} - \widehat{\tau}_{ij}, \tag{B1}$$

where $\tau_{ij} = \overline{u_i u_j} - \overline{u}_i \overline{u}_j$ is the subgrid stress, $L_{ij} = \widehat{\overline{u_i}\overline{u_j}} - \widehat{\overline{u}}_i \widehat{\overline{u}}_j$ is the resolved turbulent stress and $T_{ij} = \widehat{\overline{u_i u_j}} - \widehat{\overline{u}}_i \widehat{\overline{u}}_j$ is the subgrid stress with respect to the combined filter $\widehat{\overline{(\cdot)}}$. Another option is to apply the Germano identity for the divergence of the subgrid vorticity flux (Maulik & San, 2016, 2017a, 2017c):

$$l = \Sigma - \widehat{\sigma}, \tag{B2}$$

where $l = -\mathrm{div}(l_j) \equiv -\frac{\partial l_j}{\partial x_j}$, $\Sigma = -\mathrm{div}(\Sigma_j)$, $\sigma = -\mathrm{div}(\sigma_j)$. The formulation of the Smagorinsky model can also be different. For example, Pawar et al. (2020) use $\tau_{ij} \approx \tau_{ij}^{Smag} \equiv -2C_S^2 \overline{\Delta}^2 |\overline{S}| \overline{S}_{ij}$ which is not equivalent to our Smagorinsky model (Equation 14) because $|\overline{S}|$ varies spatially.

In this section, we show how the formulations of the Germano identity and the Smagorinsky model influence the performance of the DSM model. We consider the Smagorinsky model of the subgrid stress $\tau_{ij} \approx \tau_{ij}^{Smag}$. The corresponding dynamic estimation of the Smagorinsky coefficient is given by:

$$C_S^2 = \frac{\langle L_{ij} M_{ij} \rangle}{\langle M_{ij} M_{ij} \rangle}, \tag{B3}$$

where $M_{ij} = -2\widehat{\overline{\Delta}}^2 |\widehat{\overline{S}}| \widehat{\overline{S}}_{ij} + 2\widehat{\overline{\Delta}^2 |\overline{S}| \overline{S}_{ij}}$. Our LES Equation 3 needs the subgrid vorticity flux which we compute as follows: $\sigma_j = \mathrm{curl}(\tau_{ij}) \equiv \left(\partial_{x_1} \tau_{12} - \partial_{x_2} \tau_{11}, \partial_{x_1} \tau_{22} - \partial_{x_2} \tau_{12}\right)$, see Anstey and Zanna (2017). We introduce two additional procedures to estimate the C_S in τ_{ij}^{Smag} dynamically via considering the Germano identities for the subgrid vorticity flux (Equation 15) and for its divergence (Equation B2), respectively:
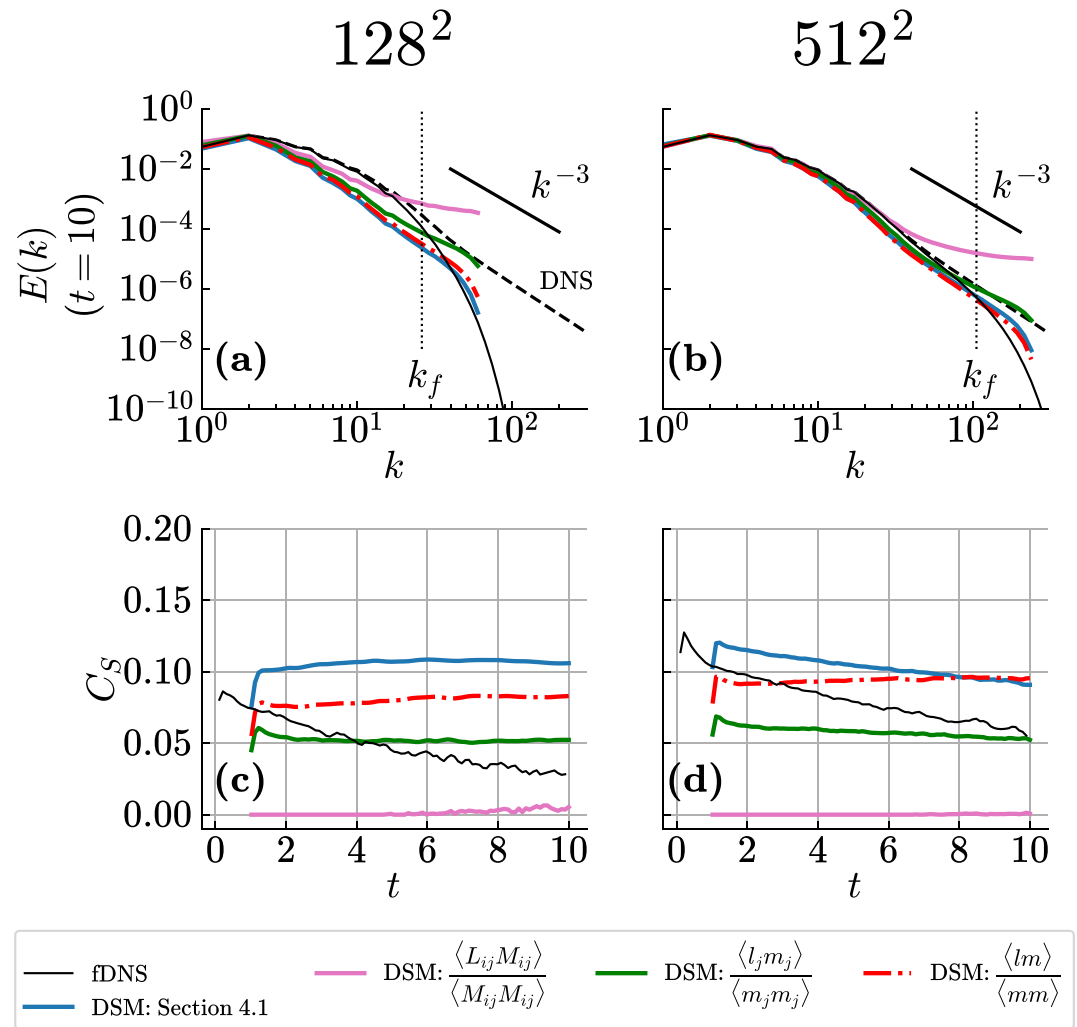
Figure B2. A posteriori experiments with the dynamic Smagorinsky model having different formulations of the Smagorinsky model and the Germano identity. Upper row: kinetic energy spectrum. Lower row: the Smagorinsky coefficient; the black line shows the C_S diagnosed a priori (Equation 26).

$$C_S^2 = \frac{\langle l_j m_j \rangle}{\langle m_j m_j \rangle}, \text{ where } m_j = \text{curl}(M_{ij}), \tag{B4}$$

$$C_S^2 = \frac{\langle lm \rangle}{\langle mm \rangle}, \text{ where } m = -\text{div}(m_j). \tag{B5}$$

In Figure B2, we compare the three described above DSM models (Equations B3–B5) to the DSM model introduced in Section 4.1. The DSM model approximating the subgrid stress (Equation B3) predominantly predicts a negative Smagorinsky coefficient which we clip to zero (Figure B2, lower row). This model is almost identical to the unparameterized simulation ($\sigma_j = 0$). The predicted C_S^2 is negative because in the decaying 2D turbulence the subgrid stress energizes the resolved eddies and thus it is correlated with the strain-rate tensor $\left(-\langle \tau_{ij} \overline{S}_{ij} \rangle < 0\right)$ which is only possible when the C_S^2 is negative. Practical computations with this model are only possible when the local clipping of $L_{ij}M_{ij}$ prior to the spatial averaging is used (Guan, Chattopadhyay, et al., 2022; Pawar et al., 2020). The dynamic model for the subgrid vorticity flux (Equation B4) helps to predict the positive Smagorinsky coefficient although the build-up of the numerical noise near the grid scale remains (Figure B2, upper row). Finally, the dynamic model for the divergence of the subgrid vorticity flux (Equation B5) leads to a further increase in the C_S and a reduction of the numerical noise near the grid scale. This model is the closest to the DSM proposed in Section 4.1.

The accurate predictions given by the DSM model from Section 4.1 can be explained by the combination of two factors: the pointwise alignment of this model with the enstrophy dissipation direction $\left(-\sigma_j^{DSM} \partial\overline{\omega}/\partial x_j \geq 0\right)$ and the dynamic modeling of the subgrid vorticity flux. Both factors lead to the extraction of information about the enstrophy dissipation on the test filter scale:

$$l_j \alpha_j \sim \Sigma_j \left(-\frac{\partial\widehat{\overline{\omega}}}{\partial x_j}\right) \sim \Pi_Z. \tag{B6}$$

Appendix C: Derivation of the Dynamic Models

C1. DSM Model

We first need to define the Smagorinsky model on filter scales $\overline{\Delta}$ and $\widehat{\overline{\Delta}}$, respectively:

$$\sigma_j = -C_S^2 \overline{\Delta}^2 |\overline{S}| \frac{\partial\overline{\omega}}{\partial x_j}, \tag{C1}$$

$$\Sigma_j = -C_S^2 \widehat{\overline{\Delta}}^2 |\widehat{\overline{S}}| \frac{\partial\widehat{\overline{\omega}}}{\partial x_j}, \tag{C2}$$

where we assumed that coefficient C_S is equal for both filters and spatially-independent. Then the Germano identity (Equation 15) reads as:

$$l_j = \Sigma_j - \widehat{\sigma}_j = C_S^2 \left(-\widehat{\overline{\Delta}}^2 |\widehat{\overline{S}}| \frac{\partial\widehat{\overline{\omega}}}{\partial x_j} + \widehat{\overline{\Delta}^2 |\overline{S}| \frac{\partial\overline{\omega}}{\partial x_j}}\right) = C_S^2 \alpha_j. \tag{C3}$$

In the least squares approach of Ghosal et al. (1995), we define the local error $e_j = l_j - C_S^2 \alpha_j$ and the domain-averaged error:

$$\langle e_j^2 \rangle = \langle l_j l_j \rangle + C_S^4 \langle \alpha_j \alpha_j \rangle - 2C_S^2 \langle l_j \alpha_j \rangle. \tag{C4}$$

Its minimum as a function of C_S^2 is given by:

$$C_S^2 = \frac{\langle l_j \alpha_j \rangle}{\langle \alpha_j \alpha_j \rangle}. \tag{C5}$$

C2. DMM Model

The mixed subgrid model on filter scales $\overline{\Delta}$ and $\widehat{\overline{\Delta}}$, respectively:

$$\sigma_j = \overline{\overline{u}_j \overline{\omega}} - \overline{\overline{u}}_j \overline{\overline{\omega}} + C_S^4 \overline{\Delta}^4 |\overline{S}| \frac{\partial\nabla^2\overline{\omega}}{\partial x_j}, \tag{C6}$$

$$\Sigma_j = \widehat{\overline{\widehat{\overline{u}}_j \widehat{\overline{\omega}}}} - \widehat{\overline{\widehat{\overline{u}}}}_j \widehat{\overline{\widehat{\overline{\omega}}}} + C_S^4 \widehat{\overline{\Delta}}^4 |\widehat{\overline{S}}| \frac{\partial\nabla^2\widehat{\overline{\omega}}}{\partial x_j}. \tag{C7}$$

The Germano identity (Equation 15) after grouping terms:

$$l_j = \Sigma_j - \widehat{\sigma}_j =$$

$$\widehat{\overline{\widehat{\overline{u}}_j \widehat{\overline{\omega}}}} - \widehat{\overline{\widehat{\overline{u}}}}_j \widehat{\overline{\widehat{\overline{\omega}}}} - \left(\widehat{\overline{\overline{u}_j \overline{\omega}}} - \widehat{\overline{\overline{u}}_j \overline{\overline{\omega}}}\right) + C_S^4 \left(\widehat{\overline{\Delta}}^4 |\widehat{\overline{S}}| \frac{\partial\nabla^2\widehat{\overline{\omega}}}{\partial x_j} - \widehat{\overline{\Delta}^4 |\overline{S}| \frac{\partial\nabla^2\overline{\omega}}{\partial x_j}}\right) = \tag{C8}$$

$$h_j + C_S^4 \alpha_j.$$

Similarly to the DSM model, the minimization of the spatially-averaged square of error $e_j = (l_j - h_j) - C_S^4 \alpha_j$ results in:

$$C_S^4 = \frac{\langle (l_j - h_j) \alpha_j \rangle}{\langle \alpha_j \alpha_j \rangle}. \tag{C9}$$

Appendix D: Two-Parameter Dynamic Procedure for DMM + Reynolds Model

In this section, we first give a classical two-parameter dynamic estimation of the coefficients C_S and C_R in DMM + Reynolds model (Horiuti, 1997; Salvetti & Banerjee, 1995; Wang & Bergstrom, 2005; Yuan et al., 2020), and then apply regularization proposed by Morinishi and Vasilyev (2001).

D1. Classical Two-Parameter Dynamic Model

The DMM + Reynolds model on filter scales $\overline{\Delta}$ and $\widehat{\overline{\Delta}}$ reads as, respectively:

$$\sigma_j = \overline{\overline{u_j}\,\overline{\omega}} - \overline{\overline{u}_j}\,\overline{\overline{\omega}} + C_S^4 \overline{\Delta}^4 |\overline{S}| \frac{\partial \nabla^2 \overline{\omega}}{\partial x_j} + C_R \left(\overline{\overline{u_j'}\,\overline{\omega'}} - \overline{\overline{u}_j'}\,\overline{\overline{\omega'}} \right), \tag{D1}$$

$$\Sigma_j = \widehat{\overline{\widehat{\overline{u}_j}\,\widehat{\overline{\omega}}}} - \widehat{\overline{\widehat{\overline{u}}_j}}\,\widehat{\overline{\widehat{\overline{\omega}}}} + C_S^4 \widehat{\overline{\Delta}}^4 |\widehat{\overline{S}}| \frac{\partial \nabla^2 \widehat{\overline{\omega}}}{\partial x_j} + C_R \left(\widehat{\overline{\widehat{\overline{u}_j'}\,\widehat{\overline{\omega'}}}} - \widehat{\overline{\widehat{\overline{u}}_j'}}\,\widehat{\overline{\widehat{\overline{\omega'}}}} \right), \tag{D2}$$

where for any ϕ we have: $\overline{\phi'} = \overline{\phi} - \overline{\overline{\phi}}$ and $\widehat{\overline{\phi'}} = \widehat{\overline{\phi}} - \widehat{\overline{\widehat{\overline{\phi}}}}$. The Germano identity (Equation 15) for this model after grouping terms:

$$l_j = \Sigma_j - \widehat{\sigma}_j = h_j + C_S^4 \alpha_j + C_R b_j, \tag{D3}$$

where as before $l_j = \widehat{\overline{\widehat{\overline{u}_j}\,\widehat{\overline{\omega}}}} - \widehat{\overline{\widehat{\overline{u}}_j}}\,\widehat{\overline{\widehat{\overline{\omega}}}}$, $h_j = \widehat{\overline{\widehat{\overline{u}}_j}\,\widehat{\overline{\omega}}} - \widehat{\overline{\widehat{\overline{u}}_j}}\,\widehat{\overline{\widehat{\overline{\omega}}}} - \left(\widehat{\overline{\overline{u_j}\,\overline{\omega}}} - \widehat{\overline{\overline{u}_j}\,\overline{\overline{\omega}}} \right)$, $\alpha_j = \widehat{\overline{\Delta}}^4 |\widehat{\overline{S}}| \frac{\partial \nabla^2 \widehat{\overline{\omega}}}{\partial x_j} - \widehat{\overline{\Delta}^4 |\overline{S}| \frac{\partial \nabla^2 \overline{\omega}}{\partial x_j}}$ and

$$b_j = \widehat{\overline{\widehat{\overline{u}_j'}\,\widehat{\overline{\omega'}}}} - \widehat{\overline{\widehat{\overline{u}}_j'}}\,\widehat{\overline{\widehat{\overline{\omega'}}}} - \left(\widehat{\overline{\overline{u_j'}\,\overline{\omega'}}} - \widehat{\overline{\overline{u}_j'}\,\overline{\overline{\omega'}}} \right). \tag{D4}$$

We define the local error in Germano identity $e_j = (l_j - h_j) - C_R b_j - C_S^4 \alpha_j$ and consider its minimization:

$$\frac{\partial}{\partial C_R} \langle e_j e_j \rangle = 0 \rightarrow C_R \langle b_j b_j \rangle + C_S^4 \langle \alpha_j b_j \rangle = \langle (l_j - h_j) b_j \rangle, \tag{D5}$$

$$\frac{\partial}{\partial C_S^4} \langle e_j e_j \rangle = 0 \rightarrow C_R \langle b_j \alpha_j \rangle + C_S^4 \langle \alpha_j \alpha_j \rangle = \langle (l_j - h_j) \alpha_j \rangle. \tag{D6}$$

The solution to the above equations predicts both parameters C_S and C_R:

$$C_R = \frac{\langle (l_j - h_j) b_j \rangle \langle \alpha_j \alpha_j \rangle - \langle (l_j - h_j) \alpha_j \rangle \langle \alpha_j b_j \rangle}{\langle \alpha_j \alpha_j \rangle \langle b_j b_j \rangle - \langle \alpha_j b_j \rangle^2}, \tag{D7}$$

$$C_S^4 = \frac{\langle (l_j - h_j) \alpha_j \rangle \langle b_j b_j \rangle - \langle (l_j - h_j) b_j \rangle \langle \alpha_j b_j \rangle}{\langle \alpha_j \alpha_j \rangle \langle b_j b_j \rangle - \langle \alpha_j b_j \rangle^2}. \tag{D8}$$
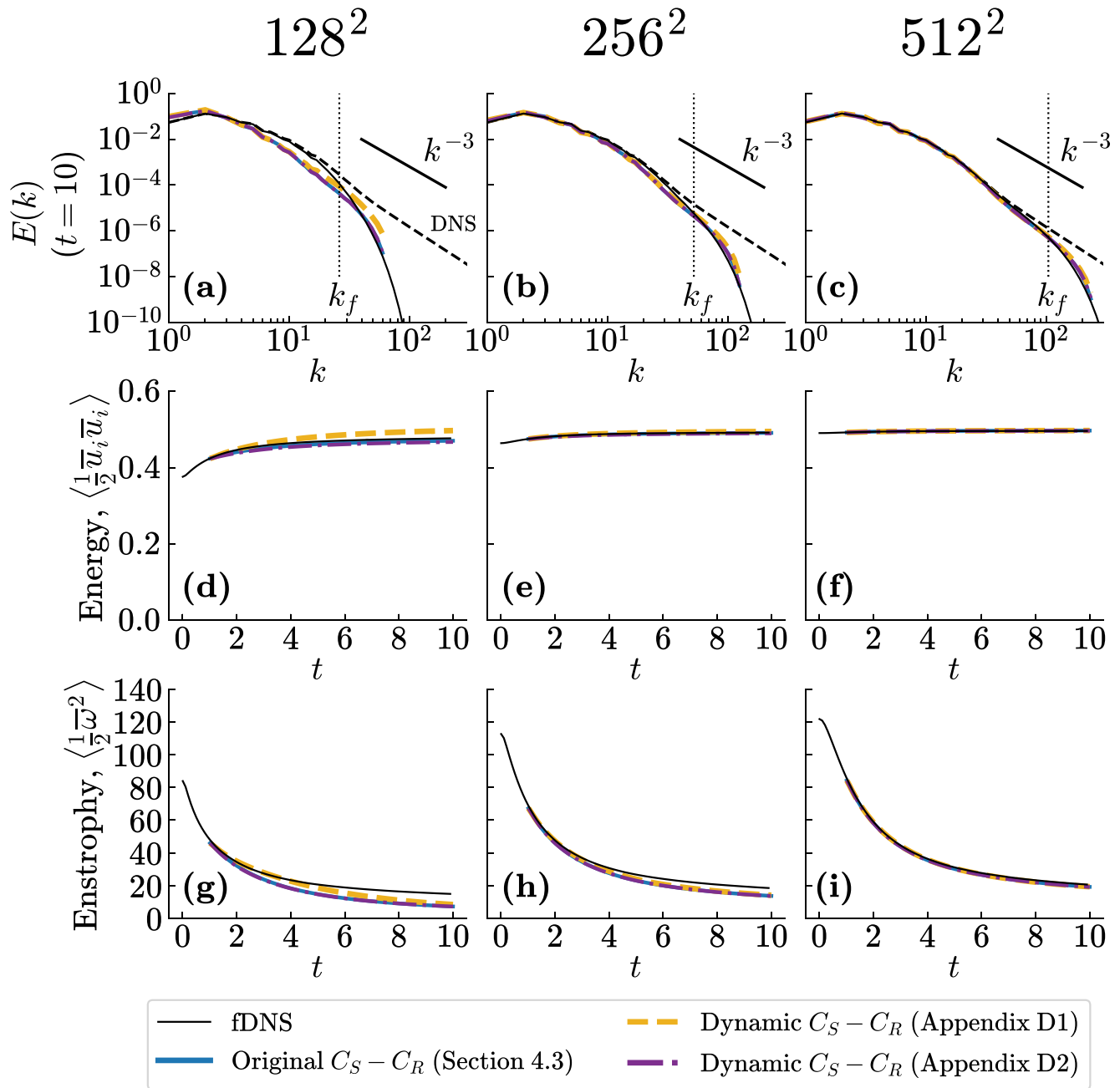
Figure D1. A posteriori experiments in decaying turbulence problem (similar to Figure 7) with the subgrid model DMM + Reynolds, where parameters C_S and C_R are estimated in different ways summarized in the legend.

D2. Regularization

Morinishi and Vasilyev (2001) found that the condition number of system of Equations D5 and D6 may be too large and may result to unstable inversion. The regularization consists in approximation of the full system by the upper-triangular matrix:

$$\begin{bmatrix} \langle b_j b_j \rangle & \langle \alpha_j b_j \rangle \\ 0 & \langle \alpha_j \alpha_j \rangle \end{bmatrix} \begin{bmatrix} C_R \\ C_S^4 \end{bmatrix} = \begin{bmatrix} \langle (l_j - h_j) b_j \rangle \\ \langle (l_j - h_j) \alpha_j \rangle \end{bmatrix}. \tag{D9}$$
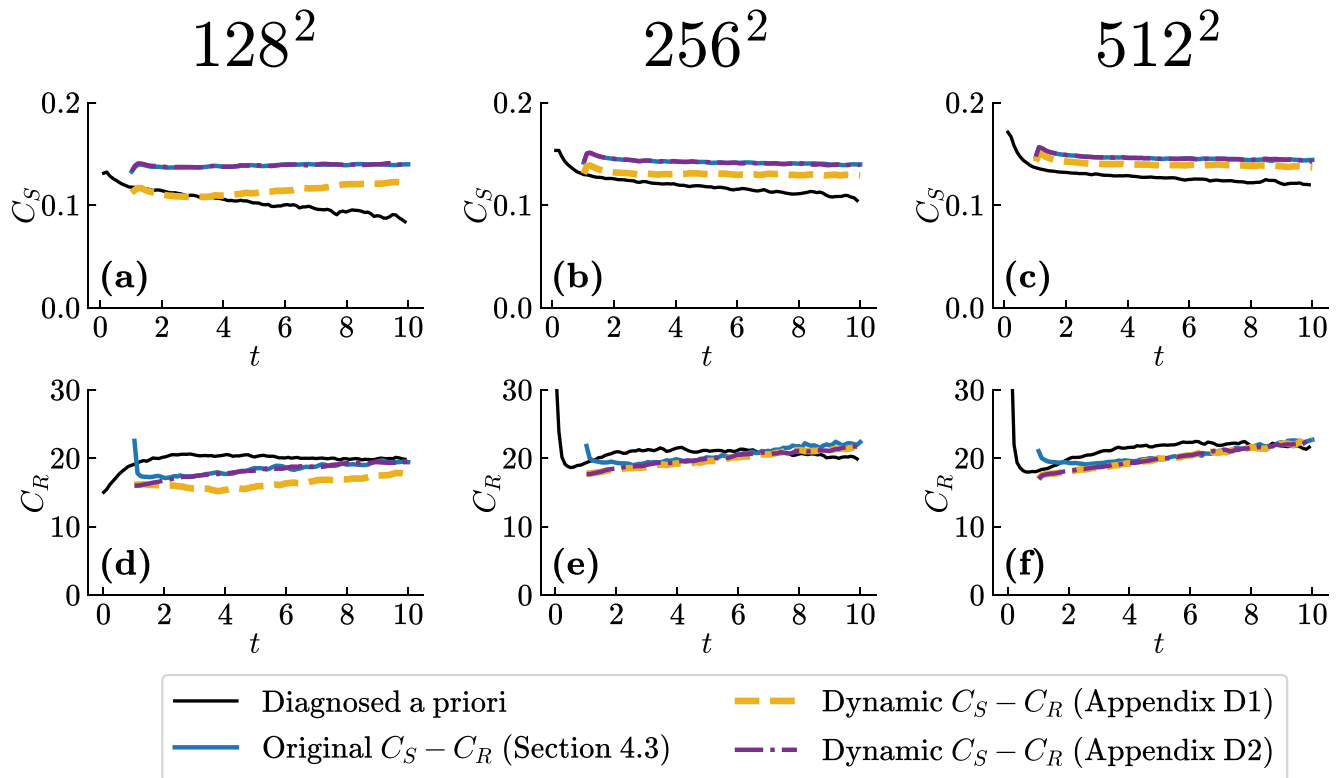
Figure D2. Coefficients C_S and C_R in DMM + Reynolds model. Black line: coefficients diagnosed from Direct numerical simulation data by least squares fit of subgrid flux. Color lines: coefficients predicted in a posteriori experiments.

The second line of Equation D9 gives the Smagorinsky parameter exactly the same way as DMM model (Equation C9). The second parameter C_R can be stably computed as C_S is known:

$$C_R = \frac{\langle (l_j - h_j)b_j \rangle - C_S^4 \langle \alpha_j b_j \rangle}{\langle b_j b_j \rangle}. \tag{D10}$$

We note that the originally proposed DMM + Reynolds model (Section 4.3) also determines coefficients C_S and C_R sequentially, and is different only in the stage of determining C_R.

D3. Experiments

In Figure D1 we show a posteriori experiments with three variants of DMM + Reynolds model, where parameters C_S and C_R are estimated as originally proposed (Section 4.3) or with the two-parameter dynamic procedures (D1 and D2 in Appendix D). We observe that in general the performance of two-parameter dynamic procedure in both variants is similar to the originally proposed DMM + Reynolds model in the presented statistics. Our main concern is the performance of the dynamic model given in D1 in Appendix D at the coarsest resolution: it overestimates energy growth (Figure D1d) and tends to produce numerical noise near the grid scale (Figure D1a). The regularized dynamic model (D2 in Appendix D) efficiently removes this drawback and is almost similar to the originally proposed DMM + Reynolds model. Our findings can be explained by the analysis of the predicted coefficients C_S and C_R (Figure D2). The regularized dynamic model (D2 in Appendix D) predicts both coefficients C_S and C_R closely to the originally proposed DMM + Reynolds model for a range of resolutions. The classical dynamic model (D1 in Appendix D) underestimates the Smagorinsky coefficient at the coarsest resolution (Figure D2a) and it results in the formation of the numerical noise.

Data Availability Statement

The software of the barotropic model in C++, QG model in Python and NEMO model in Fortran with implemented parameterizations are available via Zenodo (Perezhogin & Glazunov, 2023), where we also provide simulation data and Figure plotting functions.

References

Abernathey, R., Rocha, C. B., Ross, A., Jansen, M., Li, Z., Poulin, F. J., et al. (2022). pyqg/pyqg: V0.7.2. *Zenodo.* https://doi.org/10.5281/zenodo.6563667

Adcock, S. T., & Marshall, D. P. (2000). Interactions between geostrophic eddies and the mean circulation over large-scale bottom topography. *Journal of Physical Oceanography*, *30*(12), 3223–3238. https://doi.org/10.1175/1520-0485(2000)030<3223:ibgeat>2.0.co;2

Adcroft, A., Anderson, W., Balaji, V., Blanton, C., Bushuk, M., Dufour, C. O., et al. (2019). The gfdl global ocean and sea ice model om4. 0: Model description and simulation features. *Journal of Advances in Modeling Earth Systems*, *11*(10), 3167–3211. https://doi.org/10.1029/2019ms001726

Anstey, J. A., & Zanna, L. (2017). A deformation-based parametrization of ocean mesoscale eddy Reynolds stresses. *Ocean Modelling*, *112*, 99–111. https://doi.org/10.1016/j.ocemod.2017.02.004

Arakawa, A. (1997). Computational design for long-term numerical integration of the equations of fluid motion: Two-dimensional incompressible flow. Part I. *Journal of Computational Physics*, *135*(2), 103–114. https://doi.org/10.1006/jcph.1997.5697

Bachman, S. D. (2019). The GM+ E closure: A framework for coupling backscatter with the gent and mcwilliams parameterization. *Ocean Modelling*, *136*, 85–106. https://doi.org/10.1016/j.ocemod.2019.02.006

Bachman, S. D., Anstey, J. A., & Zanna, L. (2018). The relationship between a deformation-based eddy parameterization and the lans-α turbulence model. *Ocean Modelling*, *126*, 56–62. https://doi.org/10.1016/j.ocemod.2018.04.007

Bachman, S. D., Fox-Kemper, B., & Pearson, B. (2017). A scale-aware subgrid model for quasi-geostrophic turbulence. *Journal of Geophysical Research: Oceans*, *122*(2), 1529–1554. https://doi.org/10.1002/2016jc012265

Bardina, J., Ferziger, J., & Reynolds, W. (1980). Improved subgrid-scale models for large-eddy simulation. In *13th fluid and plasmadynamics conference* (p. 1357).

Bardino, J., Ferziger, J. H., & Reynolds, W. C. (1983). *Improved turbulence models based on large eddy simulation of homogeneous, incompressible turbulent flows*. Stanford University Report.

Batchelor, G. K. (1969). Computation of the energy spectrum in homogeneous two-dimensional turbulence. *The Physics of Fluids*, *12*(12), 233–II-239. https://doi.org/10.1063/1.1692443

Bolton, T., & Zanna, L. (2019). Applications of deep learning to ocean data inference and subgrid parameterization. *Journal of Advances in Modeling Earth Systems*, *11*(1), 376–399. https://doi.org/10.1029/2018ms001472

Borue, V., & Orszag, S. A. (1998). Local energy flux and subgrid-scale statistics in three-dimensional turbulence. *Journal of Fluid Mechanics*, *366*, 1–31. https://doi.org/10.1017/s0022112097008306

Bose, S. T., Moin, P., & You, D. (2010). Grid-independent large-eddy simulation using explicit filtering. *Physics of Fluids*, *22*(10), 105103. https://doi.org/10.1063/1.3485774

Bouchet, F. (2003). Parameterization of two-dimensional turbulence using an anisotropic maximum entropy production principle. *arXiv preprint cond-mat/0305205*.

Brun, C., & Friedrich, R. (2001). Modeling the test SGS tensor T_{ij}: An issue in the dynamic approach. *Physics of Fluids*, *13*(8), 2373–2385. https://doi.org/10.1063/1.1378037

Buxton, O., Laizet, S., & Ganapathisubramani, B. (2011). The interaction between strain-rate and rotation in shear flow turbulence from inertial range to dissipative length scales. *Physics of Fluids*, *23*(6), 061704. https://doi.org/10.1063/1.3599080

Cabanes, C., Lee, T., & Fu, L.-L. (2008). Mechanisms of interannual variations of the meridional overturning circulation of the North Atlantic Ocean. *Journal of Physical Oceanography*, *38*(2), 467–480. https://doi.org/10.1175/2007jpo3726.1

Carati, D., Winckelmans, G. S., & Jeanmart, H. (2001). On the modelling of the subgrid-scale and filtered-scale stress tensors in large-eddy simulation. *Journal of Fluid Mechanics*, *441*, 119–138. https://doi.org/10.1017/s0022112001004773

Charney, J. G. (1971). Geostrophic turbulence. *Journal of the Atmospheric Sciences*, *28*(6), 1087–1095. https://doi.org/10.1175/1520-0469(1971)028<1087:gt>2.0.co;2

Chen, S., Ecke, R. E., Eyink, G. L., Rivera, M., Wan, M., & Xiao, Z. (2006). Physical mechanism of the two-dimensional inverse energy cascade. *Physical Review Letters*, *96*(8), 084502. https://doi.org/10.1103/physrevlett.96.084502

Chen, S., Ecke, R. E., Eyink, G. L., Wang, X., & Xiao, Z. (2003). Physical mechanism of the two-dimensional enstrophy cascade. *Physical Review Letters*, *91*(21), 214501. https://doi.org/10.1103/physrevlett.91.214501

Chow, F. K., & Moin, P. (2003). A further study of numerical errors in large-eddy simulations. *Journal of Computational Physics*, *184*(2), 366–380. https://doi.org/10.1016/s0021-9991(02)00020-7

Clark, R. A., Ferziger, J. H., & Reynolds, W. C. (1979). Evaluation of subgrid-scale models using an accurately simulated turbulent flow. *Journal of Fluid Mechanics*, *91*(1), 1–16. https://doi.org/10.1017/s002211207900001x

Eden, C., & Greatbatch, R. J. (2008). Towards a mesoscale eddy closure. *Ocean Modelling*, *20*(3), 223–239. https://doi.org/10.1016/j.ocemod.2007.09.002

Ferrari, R., & Wunsch, C. (2009). Ocean circulation kinetic energy: Reservoirs, sources, and sinks. *Annual Review of Fluid Mechanics*, *41*(1), 253–282. https://doi.org/10.1146/annurev.fluid.40.111406.102139

Fox-Kemper, B., & Menemenlis, D. (2008). Can large eddy simulation techniques improve mesoscale rich ocean models. *Ocean Modeling in an Eddying Regime*, *177*, 319–337.

Frederiksen, J. S., & Davies, A. G. (1997). Eddy viscosity and stochastic backscatter parameterizations on the sphere for atmospheric circulation models. *Journal of the Atmospheric Sciences*, *54*(20), 2475–2492. https://doi.org/10.1175/1520-0469(1997)054<2475:evasbp>2.0.co;2

Frederiksen, J. S., O'Kane, T. J., & Zidikheri, M. J. (2012). Stochastic subgrid parameterizations for atmospheric and oceanic flows. *Physica Scripta*, *85*(6), 068202. https://doi.org/10.1088/0031-8949/85/06/068202

Frezat, H., Le Sommer, J., Fablet, R., Balarac, G., & Lguensat, R. (2022). A posteriori learning for quasi-geostrophic turbulence parametrization. *Journal of Advances in Modeling Earth Systems*, *14*(11), e2022MS003124. https://doi.org/10.1029/2022ms003124

Gent, P. R., & Mcwilliams, J. C. (1990). Isopycnal mixing in ocean circulation models. *Journal of Physical Oceanography*, *20*(1), 150–155. https://doi.org/10.1175/1520-0485(1990)020<0150:imiocm>2.0.co;2

Germano, M. (1986). A proposal for a redefinition of the turbulent stresses in the filtered Navier–Stokes equations. *The Physics of Fluids*, *29*(7), 2323–2324. https://doi.org/10.1063/1.865568

Germano, M. (1992). Turbulence: The filtering approach. *Journal of Fluid Mechanics*, *238*, 325–336. https://doi.org/10.1017/s0022112092001733

Germano, M., Piomelli, U., Moin, P., & Cabot, W. H. (1991). A dynamic subgrid-scale eddy viscosity model. *Physics of Fluids A: Fluid Dynamics*, *3*(7), 1760–1765. https://doi.org/10.1063/1.857955

Ghosal, S. (1996). An analysis of numerical errors in large-eddy simulations of turbulence. *Journal of Computational Physics*, *125*(1), 187–206. https://doi.org/10.1006/jcph.1996.0088

Ghosal, S., Lund, T. S., Moin, P., & Akselvoll, K. (1995). A dynamic localization model for large-eddy simulation of turbulent flows. *Journal of Fluid Mechanics*, *286*, 229–255. https://doi.org/10.1017/s0022112095000711

Graham, J. P., & Ringler, T. (2013). A framework for the evaluation of turbulence closures used in mesoscale ocean large-eddy simulations. *Ocean Modelling*, *65*, 25–39. https://doi.org/10.1016/j.ocemod.2013.01.004

Greatbatch, R. J. (1998). Exploring the relationship between eddy-induced transport velocity, vertical momentum transfer, and the isopycnal flux of potential vorticity. *Journal of Physical Oceanography*, *28*(3), 422–432. https://doi.org/10.1175/1520-0485(1998)028<0422:etrbei>2.0.co;2

Grooms, I., Lee, Y., & Majda, A. J. (2015). Numerical schemes for stochastic backscatter in the inverse cascade of quasigeostrophic turbulence. *Multiscale Modeling and Simulation*, *13*(3), 1001–1021. https://doi.org/10.1137/140990048

Grooms, I., Nadeau, L.-P., & Smith, K. S. (2013). Mesoscale eddy energy locality in an idealized ocean model. *Journal of Physical Oceanography*, *43*(9), 1911–1923. https://doi.org/10.1175/jpo-d-13-036.1

Guan, Y., Chattopadhyay, A., Subel, A., & Hassanzadeh, P. (2022). Stable a posteriori les of 2d turbulence using convolutional neural networks: Backscattering analysis and generalization to higher re via transfer learning. *Journal of Computational Physics*, *458*, 111090. https://doi.org/10.1016/j.jcp.2022.111090

Guan, Y., Subel, A., Chattopadhyay, A., & Hassanzadeh, P. (2022). Learning physics-constrained subgrid-scale closures in the small-data regime for stable and accurate les. *Physica D: Nonlinear Phenomena*, *443*, 133568. https://doi.org/10.1016/j.physd.2022.133568

Guillaumin, A. P., & Zanna, L. (2021). Stochastic-deep learning parameterization of ocean momentum forcing. *Journal of Advances in Modeling Earth Systems*, *13*(9), e2021MS002534. https://doi.org/10.1029/2021ms002534

Gullbrand, J., & Chow, F. K. (2003). The effect of numerical errors and turbulence models in large-eddy simulations of channel flow, with and without explicit filtering. *Journal of Fluid Mechanics*, *495*, 323–341. https://doi.org/10.1017/s0022112003006268

Haarsma, R. J., Roberts, M. J., Vidale, P. L., Senior, C. A., Bellucci, A., Bao, Q., et al. (2016). High resolution model intercomparison project (highresmip v1. 0) for CMIP6. *Geoscientific Model Development*, *9*(11), 4185–4208. https://doi.org/10.5194/gmd-9-4185-2016

Hewitt, H. T., Roberts, M., Mathiot, P., Biastoch, A., Blockley, E., Chassignet, E. P., et al. (2020). Resolving and parameterising the ocean mesoscale in earth system models. *Current Climate Change Reports*, *6*(4), 1–16. https://doi.org/10.1007/s40641-020-00164-w

Horiuti, K. (1997). A new dynamic two-parameter mixed model for large-eddy simulation. *Physics of Fluids*, *9*(11), 3443–3464. https://doi.org/10.1063/1.869454

Jakhar, K., Guan, Y., Mojgani, R., Chattopadhyay, A., Hassanzadeh, P., & Zanna, L. (2023). Learning closed-form equations for subgrid-scale closures from high-fidelity data: Promises and challenges. *arXiv preprint arXiv:2306.05014*.

Jansen, M. F., Adcroft, A., Khani, S., & Kong, H. (2019). Toward an energetically consistent, resolution aware parameterization of ocean mesoscale eddies. *Journal of Advances in Modeling Earth Systems*, *11*(8), 2844–2860. https://doi.org/10.1029/2019ms001750

Jansen, M. F., & Held, I. M. (2014). Parameterizing subgrid-scale eddy effects using energetically consistent backscatter. *Ocean Modelling*, *80*, 36–48. https://doi.org/10.1016/j.ocemod.2014.06.002

Jansen, M. F., Held, I. M., Adcroft, A., & Hallberg, R. (2015). Energy budget-based backscatter in an eddy permitting primitive equation model. *Ocean Modelling*, *94*, 15–26. https://doi.org/10.1016/j.ocemod.2015.07.015

Juricke, S., Bellinghausen, K., Danilov, S., Kutsenko, A., & Oliver, M. (2023). Scale analysis on unstructured grids: Kinetic energy and dissipation power spectra on triangular meshes. *Journal of Advances in Modeling Earth Systems*, *15*(1), e2022MS003280. https://doi.org/10.1029/2022ms003280

Juricke, S., Danilov, S., Koldunov, N., Oliver, M., & Sidorenko, D. (2020). Ocean kinetic energy backscatter parametrization on unstructured grids: Impact on global eddy-permitting simulations. *Journal of Advances in Modeling Earth Systems*, *12*(1), e2019MS001855. https://doi.org/10.1029/2019ms001855

Juricke, S., Danilov, S., Kutsenko, A., & Oliver, M. (2019). Ocean kinetic energy backscatter parametrizations on unstructured grids: Impact on mesoscale turbulence in a channel. *Ocean Modelling*, *138*, 51–67. https://doi.org/10.1016/j.ocemod.2019.03.009

Khani, S., & Dawson, C. N. (2023). A gradient based subgrid-scale parameterization for ocean mesoscale eddies. *Journal of Advances in Modeling Earth Systems*, *15*(2), e2022MS003356. https://doi.org/10.1029/2022ms003356

Khani, S., Jansen, M. F., & Adcroft, A. (2019). Diagnosing subgrid mesoscale eddy fluxes with and without topography. *Journal of Advances in Modeling Earth Systems*, *11*(12), 3995–4015. https://doi.org/10.1029/2019ms001721

Kraichnan, R. H. (1967). Inertial ranges in two-dimensional turbulence. *The Physics of Fluids*, *10*(7), 1417–1423. https://doi.org/10.1063/1.1762301

Kraichnan, R. H. (1976). Eddy viscosity in two and three dimensions. *Journal of the Atmospheric Sciences*, *33*(8), 1521–1536. https://doi.org/10.1175/1520-0469(1976)033<1521:evitat>2.0.co;2

Langford, J. A., & Moser, R. D. (1999). Optimal les formulations for isotropic turbulence. *Journal of Fluid Mechanics*, *398*, 321–346. https://doi.org/10.1017/s0022112099006369

Layton, W. J., & Rebholz, L. G. (2012). *Approximate deconvolution models of turbulence: Analysis, phenomenology and numerical analysis* (Vol. 2042). Springer Science & Business Media.

Leith, C. (1996). Stochastic models of chaotic systems. *Physica D: Nonlinear Phenomena*, *98*(2–4), 481–491. https://doi.org/10.1016/0167-2789(96)00107-8

Leith, C. E. (1968). Diffusion approximation for two-dimensional turbulence. *The Physics of Fluids*, *11*(3), 671–672. https://doi.org/10.1063/1.1691968

Leonard, A. (1975). Energy cascade in large-eddy simulations of turbulent fluid flows. In *Advances in geophysics* (Vol. 18, pp. 237–248). Elsevier.

Lévy, M., Klein, P., Tréguier, A.-M., Iovino, D., Madec, G., Masson, S., & Takahashi, K. (2010). Modifications of gyre circulation by sub-mesoscale physics. *Ocean Modelling*, *34*(1–2), 1–15. https://doi.org/10.1016/j.ocemod.2010.04.001

Loose, N., Bachman, S., Grooms, I., & Jansen, M. (2023). Diagnosing scale-dependent energy cycles in a high-resolution isopycnal ocean model. *Journal of Physical Oceanography*, *53*(1), 157–176. https://doi.org/10.1175/jpo-d-22-0083.1

Lund, T. (1997). On the use of discrete filters for large eddy simulation. *Annual Research Briefs*, 83–95.

Lund, T. (2003). The use of explicit filters in large eddy simulation. *Computers & Mathematics with Applications*, *46*(4), 603–616. https://doi.org/10.1016/s0898-1221(03)90019-8

Lund, T. S., & Novikov, E. (1992). *Parameterization of subgrid-scale stress by the velocity gradient tensor*. Center for Turbulence Research Annual Research Briefs.

Madec, G., & the NEMO Team. (2008). *Nemo ocean engine (Note du Pôle de modélisation No. 27)*. Institut Pierre-Simon Laplace (IPSL).

Mana, P. P., & Zanna, L. (2014). Toward a stochastic parameterization of ocean mesoscale eddies. *Ocean Modelling*, *79*, 1–20. https://doi.org/10.1016/j.ocemod.2014.04.002

Marshall, D. P., & Adcroft, A. J. (2010). Parameterization of ocean eddies: Potential vorticity mixing, energetics and Arnold's first stability theorem. *Ocean Modelling*, *32*(3–4), 188–204. https://doi.org/10.1016/j.ocemod.2010.02.001

Marshall, D. P., Maddison, J. R., & Berloff, P. S. (2012). A framework for parameterizing eddy potential vorticity fluxes. *Journal of Physical Oceanography*, *42*(4), 539–557. https://doi.org/10.1175/jpo-d-11-048.1

Maulik, R., & San, O. (2016). Dynamic modeling of the horizontal eddy viscosity coefficient for quasigeostrophic ocean circulation problems. *Journal of Ocean Engineering and Science*, *1*(4), 300–324. https://doi.org/10.1016/j.joes.2016.08.002

Maulik, R., & San, O. (2017a). A dynamic framework for functional parameterisations of the eddy viscosity coefficient in two-dimensional turbulence. *International Journal of Computational Fluid Dynamics*, *31*(2), 69–92. https://doi.org/10.1080/10618562.2017.1287902

Maulik, R., & San, O. (2017b). A novel dynamic framework for subgrid scale parametrization of mesoscale eddies in quasigeostrophic turbulent flows. *Computers & Mathematics with Applications*, *74*(3), 420–445. https://doi.org/10.1016/j.camwa.2017.04.016

Maulik, R., & San, O. (2017c). A stable and scale-aware dynamic modeling framework for subgrid-scale parameterizations of two-dimensional turbulence. *Computers & Fluids*, *158*, 11–38. https://doi.org/10.1016/j.compfluid.2016.11.015

Meneveau, C., & Katz, J. (2000). Scale-invariance and turbulence models for large-eddy simulation. *Annual Review of Fluid Mechanics*, *32*(1), 1–32. https://doi.org/10.1146/annurev.fluid.32.1.1

Meneveau, C., & Lund, T. S. (1997). The dynamic smagorinsky model and scale-dependent coefficients in the viscous range of turbulence. *Physics of Fluids*, *9*(12), 3932–3934. https://doi.org/10.1063/1.869493

Meyers, J., Geurts, B. J., & Baelmans, M. (2003). Database analysis of errors in large-eddy simulation. *Physics of Fluids*, *15*(9), 2740–2755. https://doi.org/10.1063/1.1597683

Morinishi, Y., & Vasilyev, O. V. (2001). A recommended modification to the dynamic two-parameter mixed subgrid scale model for large eddy simulation of wall bounded turbulent flow. *Physics of Fluids*, *13*(11), 3400–3410. https://doi.org/10.1063/1.1404396

Nadiga, B. (2008). Orientation of eddy fluxes in geostrophic turbulence. *Philosophical Transactions of the Royal Society A: Mathematical, Physical & Engineering Sciences*, *366*(1875), 2489–2508. https://doi.org/10.1098/rsta.2008.0058

Partee, S., Ellis, M., Rigazzi, A., Shao, A. E., Bachman, S., Marques, G., & Robbins, B. (2022). Using machine learning at scale in numerical simulations with SmartSim: An application to ocean climate modeling. *Journal of Computational Science*, *62*, 101707. https://doi.org/10.1016/j.jocs.2022.101707

Pawar, S., San, O., Rasheed, A., & Vedula, P. (2020). A priori analysis on deep learning of subgrid-scale parameterizations for kraichnan turbulence. *Theoretical and Computational Fluid Dynamics*, *34*(4), 429–455. https://doi.org/10.1007/s00162-019-00512-z

Pearson, B., Fox-Kemper, B., Bachman, S., & Bryan, F. (2017). Evaluation of scale-aware subgrid mesoscale eddy models in a global eddy-rich model. *Ocean Modelling*, *115*, 42–58. https://doi.org/10.1016/j.ocemod.2017.05.007

Perezhogin, P. (2019). Deterministic and stochastic parameterizations of kinetic energy backscatter in the nemo ocean model in double-gyre configuration. In *IOP conference series: Earth and environmental science* (Vol. 386, p. 012025).

Perezhogin, P., & Glazunov, A. (2023). Dataset for paper Pavel Perezhogin, Andrey Glazunov "Subgrid parameterizations of ocean mesoscale eddies based on Germano decomposition" submitted to JAMES. *Zenodo*. https://doi.org/10.5281/zenodo.8277231

Perezhogin, P., Zanna, L., & Fernandez-Granda, C. (2023). Generative data-driven approaches for stochastic subgrid parameterizations in an idealized ocean model. *arXiv preprint arXiv:2302.07984*.

Perezhogin, P. A. (2020). Testing of kinetic energy backscatter parameterizations in the nemo ocean model. *Russian Journal of Numerical Analysis and Mathematical Modelling*, *35*(2), 69–82. https://doi.org/10.1515/rnam-2020-0006

Pope, S. B. (1975). A more general effective-viscosity hypothesis. *Journal of Fluid Mechanics*, *72*(2), 331–340. https://doi.org/10.1017/s0022112075003382

Porté-Agel, F., Meneveau, C., & Parlange, M. B. (2000). A scale-dependent dynamic model for large-eddy simulation: Application to a neutral atmospheric boundary layer. *Journal of Fluid Mechanics*, *415*, 261–284. https://doi.org/10.1017/s0022112000008776

Ross, A., Li, Z., Perezhogin, P., Fernandez-Granda, C., & Zanna, L. (2023). Benchmarking of machine learning ocean subgrid parameterizations in an idealized model. *Journal of Advances in Modeling Earth Systems*, *15*(1), e2022MS003258. https://doi.org/10.1029/2022ms003258

Sagaut, P. (2006). *Large eddy simulation for incompressible flows: An introduction*. Springer Science & Business Media.

Sagaut, P., & Grohens, R. (1999). Discrete filters for large eddy simulation. *International Journal for Numerical Methods in Fluids*, *31*(8), 1195–1220. https://doi.org/10.1002/(sici)1097-0363(19991230)31:8<1195::aid-fld914>3.0.co;2-h

Salmon, R. (1978). Two-layer quasi-geostrophic turbulence in a simple special case. *Geophysical & Astrophysical Fluid Dynamics*, *10*(1), 25–52. https://doi.org/10.1080/03091927808242628

Salvetti, M. V., & Banerjee, S. (1995). A priori tests of a new dynamic subgrid-scale model for finite-difference large-eddy simulations. *Physics of Fluids*, *7*(11), 2831–2847. https://doi.org/10.1063/1.868779

San, O. (2014). A dynamic eddy-viscosity closure model for large eddy simulations of two-dimensional decaying turbulence. *International Journal of Computational Fluid Dynamics*, *28*(6–10), 363–382. https://doi.org/10.1080/10618562.2014.948426

San, O., Staples, A. E., & Iliescu, T. (2013). Approximate deconvolution large eddy simulation of a stratified two-layer quasigeostrophic ocean model. *Ocean Modelling*, *63*, 1–20. https://doi.org/10.1016/j.ocemod.2012.12.007

Sarwar, M., Cleary, M., Moinuddin, K., & Thorpe, G. (2017). On linking the filter width to the boundary layer thickness in explicitly filtered large eddy simulations of wall bounded flows. *International Journal of Heat and Fluid Flow*, *65*, 73–89. https://doi.org/10.1016/j.ijheatfluidflow.2017.04.004

Schilling, O., & Zhou, Y. (2002). Analysis of spectral eddy viscosity and backscatter in incompressible, isotropic turbulence using statistical closure theory. *Physics of Fluids*, *14*(3), 1244–1258. https://doi.org/10.1063/1.1447913

Skamarock, W. C., Klemp, J. B., Dudhia, J., Gill, D. O., Barker, D. M., Duda, M. G., et al. (2008). A description of the advanced research WRF version 3. *NCAR Technical Note*, *475*, 113.

Smagorinsky, J. (1963). General circulation experiments with the primitive equations: I. The basic experiment. *Monthly Weather Review*, *91*(3), 99–164. https://doi.org/10.1175/1520-0493(1963)091<0099:gcewtp>2.3.co;2

Stolz, S., Adams, N. A., & Kleiser, L. (2001). An approximate deconvolution model for large-eddy simulation with application to incompressible wall-bounded flows. *Physics of Fluids*, *13*(4), 997–1015. https://doi.org/10.1063/1.1350896

Sullivan, P. P., Horst, T. W., Lenschow, D. H., Moeng, C.-H., & Weil, J. C. (2003). Structure of subfilter-scale fluxes in the atmospheric surface layer with application to large-eddy simulation modelling. *Journal of Fluid Mechanics*, *482*, 101–139. https://doi.org/10.1017/s0022112003004099

Thiry, O., & Winckelmans, G. (2016). A mixed multiscale model better accounting for the cross term of the subgrid-scale stress and for backscatter. *Physics of Fluids*, *28*(2), 025111. https://doi.org/10.1063/1.4941773

Thuburn, J., Kent, J., & Wood, N. (2014). Cascades, backscatter and conservation in numerical models of two-dimensional turbulence. *Quarterly Journal of the Royal Meteorological Society*, *140*(679), 626–638. https://doi.org/10.1002/qj.2166

Vallis, G. K. (2017). *Atmospheric and oceanic fluid dynamics*. Cambridge University Press.

Vreman, B., Geurts, B., & Kuerten, H. (1994). On the formulation of the dynamic mixed subgrid-scale model. *Physics of Fluids*, *6*(12), 4057–4059. https://doi.org/10.1063/1.868333

Wang, B.-C., & Bergstrom, D. J. (2005). A dynamic nonlinear subgrid-scale stress model. *Physics of Fluids*, *17*(3), 035109. https://doi.org/10.1063/1.1858511

Wardle, R., & Marshall, J. (2000). Representation of eddies in primitive equation models by a PV flux. *Journal of Physical Oceanography*, *30*(10), 2481–2503. https://doi.org/10.1175/1520-0485(2000)030<2481:roeipe>2.0.co;2

Winckelmans, G. S., Wray, A. A., Vasilyev, O. V., & Jeanmart, H. (2001). Explicit-filtering large-eddy simulation using the tensor-diffusivity model supplemented by a dynamic smagorinsky term. *Physics of Fluids*, *13*(5), 1385–1403. https://doi.org/10.1063/1.1360192

Yuan, Z., Xie, C., & Wang, J. (2020). Deconvolutional artificial neural network models for large eddy simulation of turbulence. *Physics of Fluids*, *32*(11), 115106. https://doi.org/10.1063/5.0027146

Zanna, L., & Bolton, T. (2020). Data-driven equation discovery of ocean mesoscale closures. *Geophysical Research Letters*, *47*(17), e2020GL088376. https://doi.org/10.1029/2020gl088376

Zanna, L., Mana, P. P., Anstey, J., David, T., & Bolton, T. (2017). Scale-aware deterministic and stochastic parametrizations of eddy-mean flow interaction. *Ocean Modelling*, *111*, 66–80. https://doi.org/10.1016/j.ocemod.2017.01.004